The 3D Structural Architecture of the Human Hand Area is Non-Topographic

Juliane Doehler[1,2], Alicia Northall[1,2], Peng Liu[1,2], Alessio Fracasso[3], Anastasia Chrysidou, Oliver Speck[2,4,5,6], Gabriele Lohmann[7], Thomas Wolbers[2,5], Esther Kuehn[8,1,2,5]

[1] Institute for Cognitive Neurology and Dementia Research (IKND), Medical Faculty, Otto-von-Guericke University Magdeburg, Magdeburg, Germany

[2] German Center for Neurodegenerative Diseases (DZNE), Magdeburg, Germany

[3] Institute of Neuroscience and Psychology, University of Glasgow, Glasgow, United Kingdom

[4] Department of Biomedical Magnetic Resonance (BMMR), Otto-von-Guericke-University Magdeburg, Magdeburg, Germany

[5] Center for Behavioral Brain Sciences (CBBS), Magdeburg, Germany

[6] Leibniz Institute for Neurobiology, Magdeburg, Germany

[7] Max Planck Institute for Biological Cybernetics, Tübingen, Germany

[8] Hertie Institute for Clinical Brain Research, Tübingen, Germany

Corresponding author

Juliane Doehler, M.Sc.

Institute for Cognitive Neurology and Dementia Research (IKND), Medical Faculty, Otto-von-Guericke University Magdeburg, Magdeburg, Germany

Email: juliane.doehler@med.ovgu.de

Abstract

The functional topography of the human primary somatosensory cortex (S1) hand area is a widely studied model system to understand sensory organization and plasticity. It is so far unclear whether or not the underlying 3D structural architecture also shows a topographic organization. We used 7T MRI data to quantify layer-specific myelin, iron and mineralization in relation to population receptive field maps of individual finger representations. This 3D description allowed us to identify a characteristic profile of layer-specific myelin and iron deposition in the S1 hand area, but revealed an absence of structural differences between individual finger representations, and an absence of low-myelin borders between individual fingers. Both, however, were detected between the hand and the face areas. Using markers of responsivity, precision and sensorimotor integration, we additionally phenotyped these microstructural features with respect to their relation to BOLD signal change and behavior. We conclude that the 3D structural architecture of the human hand area is non-topographic, other than in some monkey species, which suggests a high degree of flexibility for functional finger organization and plasticity in humans.

Keywords

quantitative imaging, UHF MRI, in-vivo myeloarchitecture, cortical field, parcellation, septa

Introduction

In the mammalian brain, the topographic architecture of the primary somatosensory cortex (S1) is often studied as a model system to understand cortical functional organization and plasticity (e.g. Florence et al., 1997, Feldman & Brecht, 2005, Kuehn & Pleger, 2020). Due to their clear and fine-grained architectures, the most studied topographic areas within S1 are whisker representations in rodents (Petersen, 2007, Feldman & Brecht, 2005), and hand representations in monkeys, and humans (Shoham & Grinvald, 2001, Blake et al., 2002, Kuehn et al., 2018a, Pleger et al., 2016). While the microstructural features of these areas in relation to functional map architecture have been widely studied in rodents and monkeys (e.g. Meyer et al., 2013, Welker, 1976, Welker & Woolsey, 1976, Peters, 2009, Qi & Kaas, 2004, Jain, Catania & Kaas, 1998), the microstructure of functional finger representations remains undescribed in humans. This knowledge gap prevents us from gaining a full understanding of the neuronal mechanisms that underlie topographic organization and plasticity in humans.

Physiological studies show that low-myelin borders (so-called septa) separate major body part representations (Manger et al., 1997) and finger representations in macaque monkeys (Qi & Kaas, 2004) and owl monkeys (Jain, Catania & Kaas, 1998), as well as whisker representations in rodents (Woolsey & Van der Loos, 1970). The role of such septa is complex and ranges from functional separation to sensory encoding; it has also been suggested that septa may limit cortical plasticity in S1 (Sereno, 2005). Recently, low-myelin borders have been identified in human S1 between major body part representations, which coincided with resting-state network separation (Glasser et al., 2016, Kuehn et al., 2017a). However, it is so far unknown whether such low-myelin borders also separate single finger representations in human S1, or whether the human hand area can be regarded as one, homogenous cortical field (Sereno et al., 2022).

Conceptually, this question is important because it touches on a fundamental aspect of brain organization. In the somatosensory system, unlike in the visual system, topographic representations are discontinuous. That is, major body part representations, such as the hand and the face, are distinctly represented (Sereno et al., 2022). This representation of body parts in S1 reflects the discontinuous shape of the body in the real world, where the hand and the face, for example, are spatially distant (and can move independently) even though they cover neighboring areas in S1. Therefore, it has been suggested that low-myelin borders in S1 separate representations that are nearby in the cortex but distant in the real

world (Kuehn et al., 2017a), such as the hand and face. Alternatively, low-myelin borders may separate representations that are nearby in the cortex and nearby in the real world, but that sometimes receive distinct sensory inputs, such as individual fingers. This relates to the question of whether the hand area is encoded as a full system, or whether fingers are encoded separately, which has also been discussed in the field of psychology and cognitive neuroscience (e.g. Haggard et al., 2006). Answering this question will facilitate relating cortical myeloarchitectonic features to real world features.

Parcellation-inspired techniques can be used to investigate cortex architecture not only along the surface (i.e. in two dimensions) but also in depth (i.e. in three dimensions). This allows studying the microstructural organization in reference to computationally-relevant units (Kuehn & Sereno, 2018, Kuehn & Pleger, 2020). In S1, anatomical layer IV is the input layer, where afferent information enters the cortex (Petersen, 2007, Viaene et al., 2011, Yu et al., 2019). Layer IV neural activity correlates with applied stimulus intensity (Laskov, 1995), and may therefore be linked to the degree of blood oxygenation level-dependent (BOLD) signal change during tactile stimulation (see Huber et al., 2019 on limited spatial specificity of the BOLD signal). Additionally, reduced layer IV myelin is expected to indicate the existence of septa between cortical areas (Welker & Woolsey, 1974, Welker, 1976, Kuehn et al., 2017a). Superficial S1 layers (I-III) are origin and termination of cortico-cortical connections, for example permitting communication with the primary motor cortex (M1) (Ferezou et al., 2007, Mao et al., 2011). These layers may therefore mediate sensorimotor integration and functional connectivity. Deep S1 layers (V, VI), on the other hand, primarily connect S1 with subcortical regions (Petersen & Crochet, 2013, Sherman, 2016), but also send information to layer IV (Sherman, 2016, Zhang & Deschênes, 1997), which may sharpen neuronal representations (Pleger et al., 2016). Structural differences in deep layers may therefore relate to population receptive field (pRF) sizes, and/or tactile spatial discrimination performance.

We here used parcellation-inspired techniques to characterize layer- and finger-specific structural features of the S1 hand area, and to investigate potential structural borders between finger representations. Quantitative MRI proxies were used to estimate layer-specific myelin, diamagnetic and paramagnetic tissue substances (such as calcium and iron) and overall mineralization. Participants additionally underwent a tactile stimulation protocol to obtain pRF characteristics and % signal change. We also estimated resting-state functional connectivity and used a behavioral test battery to estimate different sensorimotor

features of the hand (i.e. tactile detection, tactile spatial discrimination, sensorimotor integration). The acquired data was used to address the following research questions: (i) Are there low-myelin borders between single finger representations in human S1?, (ii) Is the human S1 hand area homogenous, or are there systematic microstructural differences between S1 finger representations?, and (iii) Are there systematic relationships between the 3D structural architecture of S1, functional features and behavioral phenotypes?

Targeting these questions provides us with critical information on the structural architecture of S1 that may explain topographic stability and/or plasticity in conditions of health and disease. It also addresses the fundamental question of how cortical myelination differences relate to real world features.

Results

Cortical 3D Profiles and Layer Definition

To study the 3D structural architecture of the human S1 hand area in reference to functional topography, we used *in vivo* 7T MRI data of healthy adults (21 to 29 years; see **Figure 1**). We used quantitative T1 (qT1) as a proxy for cortical myelin (Stüber et al., 2014, Dinse et al., 2015) and quantitative susceptibility maps (QSM) as proxies for iron (positive values, pQSM), diamagnetic tissue substances (negative values, nQSM) (Langkammer et al., 2012, Zheng et al., 2013, Hametner et al., 2018), and overall mineralization (absolute values, aQSM) (Betts et al., 2016). In addition to anatomical scans, participants were also stimulated at the fingertips of their right hand by an automated piezoelectric stimulator, using both phase-encoded and blocked designs. We focussed on investigating left S1 (contralateral to where stimulation was applied). pRF center locations as revealed by Bayesian pRF modeling were used to locate each finger in S1 (thumb: D1, index finger: D2, middle finger: D3, ring finger: D4, little finger: D5) (Liu et al., 2021).

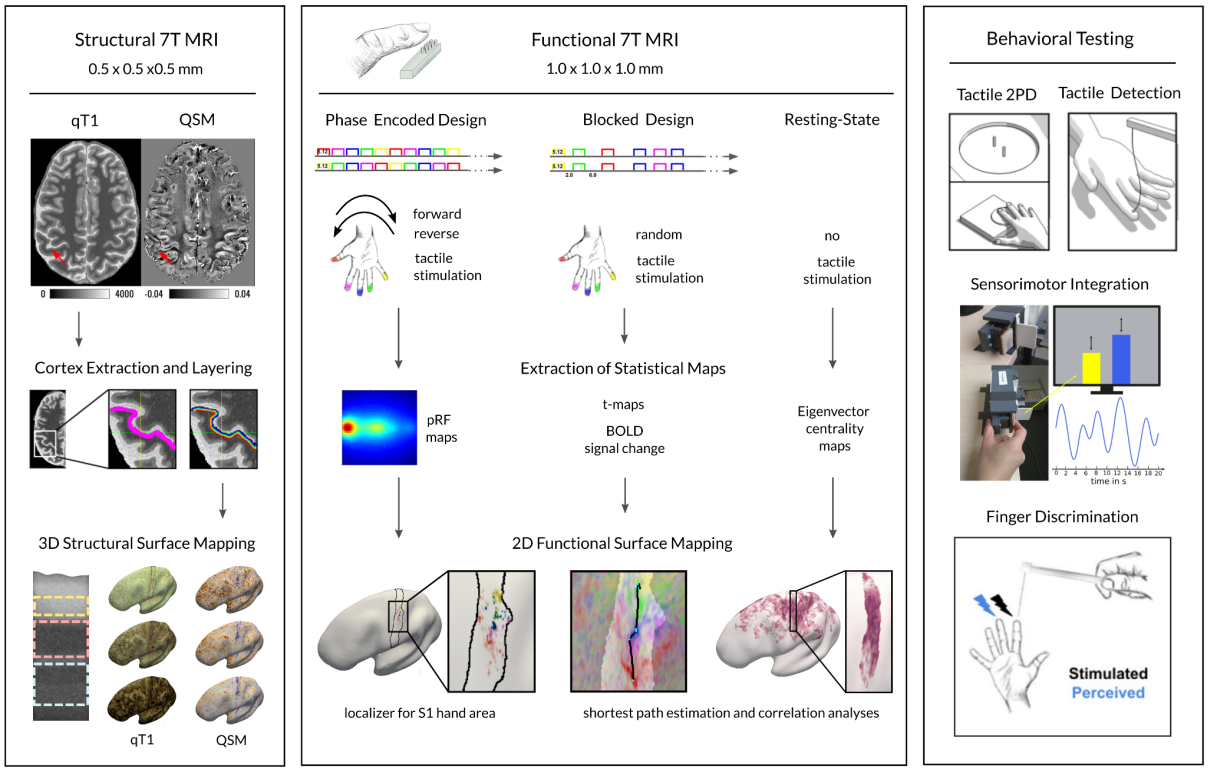

Figure 1. Overview Experimental Design. A total of n=20 participants took part in structural and functional 7T MRI data acquisition as well as in a behavioral test battery. *Left*: MP2RAGE and susceptibility-weighted imaging sequences of participants were acquired to estimate high-resolution quantitative T1 maps (qT1) and quantitative susceptibility maps (QSM), respectively. Red arrows indicate the region of interest (left S1 hand area). The MP2RAGE sequence was used to extract the cortex (magenta color), and to layer the cortex into 21 cortical

depths (rainbow color) where we sampled qT1 and QSM values to derive cortical depth-dependent profiles. These profiles were averaged into three anatomically-relevant compartments (creme: outer, light pink: middle, light blue: inner) based on *ex vivo in vivo* validated S1 data (see details below, Dinse et al., 2015). Extracted qT1 and QSM values were mapped onto the individual's inflated cortical surface. Myelin staining was remodeled according to Dinse et al. (2015). *Middle*: All participants underwent tactile stimulation during scanning using both a phase encoded design and a blocked design. Phase encoded data were used to calculate population receptive field (pRF) properties, which were used to localize the finger representations in S1, and %signal change. Blocked design data were used to calculate t-maps for shortest path estimation and BOLD signal change. Resting-state data was acquired to estimate Eigenvector centrality maps (ECMs, rectified linear unit correlation of resting-state signal fluctuations, Lohmann et al., 2018). *Right*: The behavioral test battery included tactile 2-point discrimination, tactile detection and sensorimotor integration tasks (behavioral session 1) as well as a finger discrimination task (behavioral session 2).

When extracting qT1, nQSM, pQSM and aQSM values from the S1 hand area, we obtained precise intracortical contrasts (see **Figure 2A**). As expected (Stüber et al., 2014, Dinse et al., 2015), qT1 values decrease from superficial to deep cortical depths, reflecting high myelin close to the white matter (WM). This intracortical gradient from low to high myelin is interrupted in the upper half of the profile, an area known to contain high myelin content (i.e., Baillarger band in anatomical layer IV) (Vogt, 1919, Dinse et al., 2015). Based on previous *in vivo ex vivo* validation work (Dinse et al., 2015), we used the local rate of change of qT1 values to define three anatomically-relevant cortical compartments (here referred to as 'outer layer', 'middle layer' and 'inner layer', see **Figure 2B**, **Figure 2C**), where input layer IV is assumed to be located in the middle layer, and layers V and VI are assumed to be located in the inner layer. Note that the upper peak of the pQSM profile (which showed a top-hat distribution shaped by a plateau with a double peak) is located in what we define as middle layer (containing layer IV), whereas the lower peak is located in what we define as inner layer (containing layer V). With respect to nQSM, we observed a U-shaped profile with values closest to zero in the very middle of cortical depths, which is interrupted by a small plateau in the upper half of the profile, where we expected layer IV to be located. Multi-contrast mapping therefore confirmed our qT1-based layer definition. In the main text, results are shown for these three layers (outer layer, middle layer, inner layer), while identical analyses for four equally-spaced layers are provided in the Supplemental Material (to facilitate comparing our data to previous publications, Kuehn et al., 2017a, Tardiff et al., 2015).

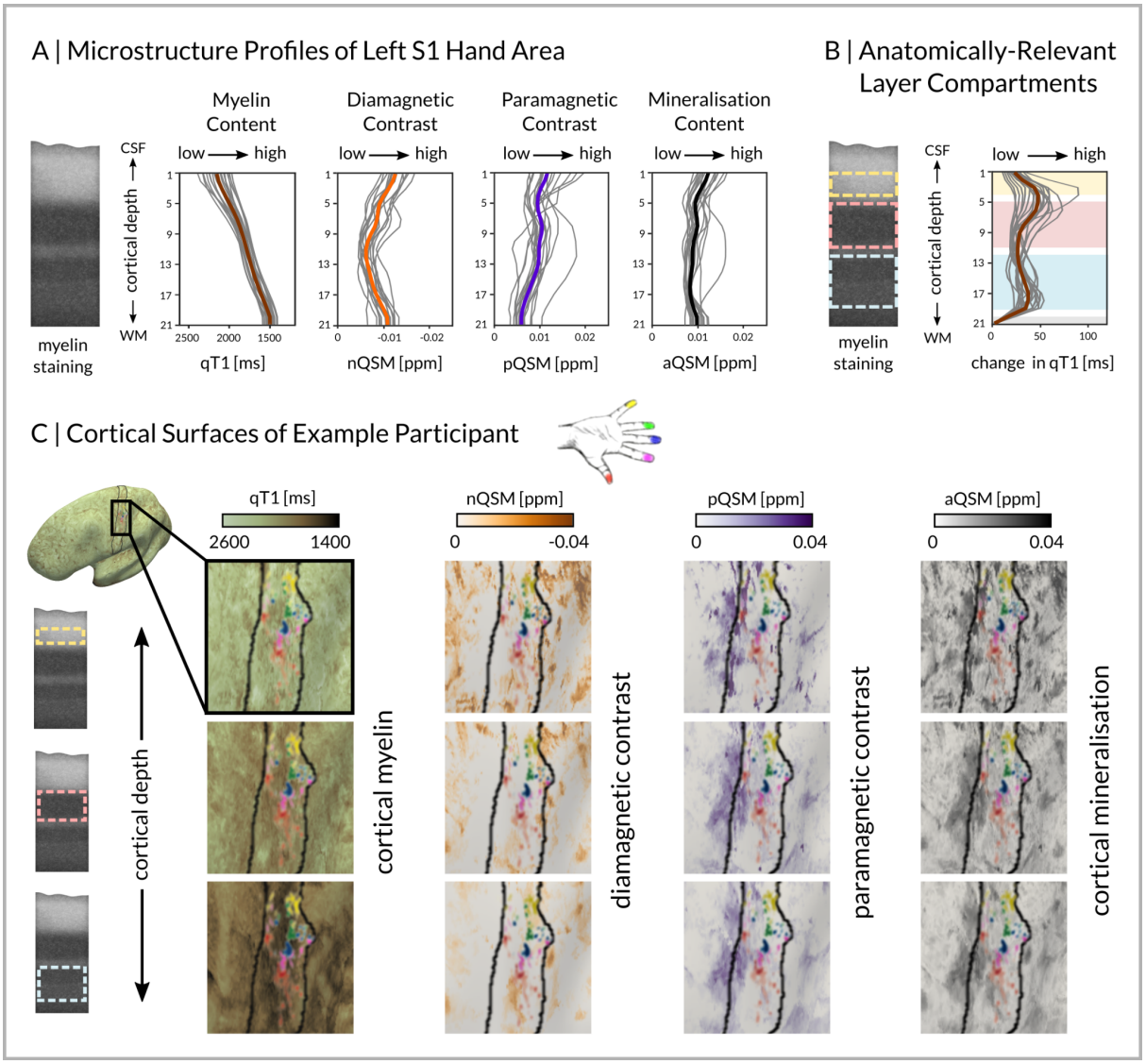

Figure 2. Cortical 3D Profiles and Layer Definition. (A) Microstructure profiles of the left (contralateral to where stimulation was applied) S1 hand area show distinct cortical depth-dependent profiles. Quantitative T1 (qT1, reflecting myelin, n=20), negative QSM (nQSM, reflecting diamagnetic tissue contrast (e.g., calcium), n=18), positive QSM (pQSM, reflecting paramagnetic tissue contrast (iron), n=18) and absolute QSM (aQSM, overall mineralization, n=18) were sampled at 21 different cortical depths (Kuehn et al., 2017a) where depth 1 is located closest to cerebrospinal fluid (CSF) and depth 21 is located closest to white matter (WM). Myelin staining was remodeled according to Dinse et al. (2015). (B) Anatomically-relevant cortical compartments (cream: 'outer layer', light pink: 'middle layer', light blue: 'inner layer') were defined based on minima and maxima of the rate of change in qT1 (first derivative of cortical depth-dependent qT1 calculated as central difference between two neighboring sampling points) that are assumed to reflect the heavily myelinated Bands of Baillarger. (C) qT1, nQSM, pQSM and aQSM values (from left to right) in the left S1 hand area in each of the layers (top row: outer layer, middle row: middle layer, bottom row: inner layer) for one example participant. The population receptive field (pRF) center is plotted on top to show individual finger representations from which data were extracted (red: thumb, magenta: index finger, blue: middle finger, green: ring finger, yellow: little finger).

Absence of Inferior-to-Superior Structural Gradient in S1 Hand Area

First, we investigated whether there is a systematic structural gradient within the S1 hand area (e.g. higher myelin in superior compared to inferior parts). To this end, we calculated layer-specific qT1, nQSM, pQSM and aQSM gradients by extracting values from inferior to superior, and compared this to zero (a value of zero indicates no systematic change along the inferior-to-superior axis). None of these tests were significant (see **Table 1** and **Figure 3**), indicating an absence of a systematic inferior-to-superior structural gradient in the S1 hand area. See **Figure 3-figure supplement 1** for results for four equally-spaced layers.

	qT1 (n=20)		**nQSM** (n=18)		**pQSM** (n=18)		**aQSM** (n=18)	
	t(19)	p	*t*(17) / W	p(*t*) / p(W)	*t*(17) / W	p(*t*) / p(W)	*t*(17)	p
outer	-2.34	0.03 **T**	-0.82 / -	0.43 / -	-0.56 / 86	0.58 / 1	0.38	0.71
middle	-1.80	0.09 **T**	-0.67 / -	0.51 / -	1.05 / -	0.31 / -	0.91	0.38
inner	0.47	0.65	1.23 / 113	0.24 / 0.25	-0.60 / -	0.56 / -	0.11	0.92

Table 1. Statistical Results of Gradient Analysis. None of the tested layer-specific structural gradient analyses (qT1, nQSM, pQSM, aQSM) were significantly different from zero. Trends above Bonferroni-corrected significance levels of p = .016 (correcting for 3 tests per variable) are marked by a T. Results are reported as Student's t (t) or Wilcoxon's W (W) for normal and non-normal distributions, respectively. Structural gradients were tested in 3 different cortical depths (outer, middle, inner).

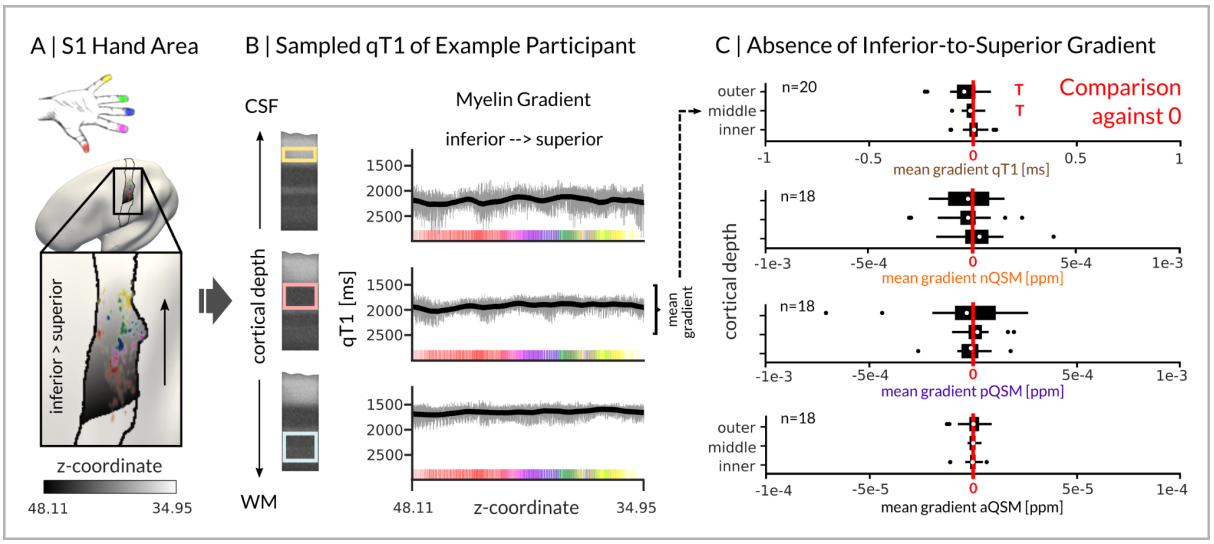

Figure 3. Absence of inferior-to-superior structural gradient in S1 hand area. (A) Using surface-based analyses, structural gradients of qT1, pQSM, nQSM and aQSM were extracted from the full finger map (=hand area) of left S1 (black lines mark anterior and posterior borders). Values were extracted from inferior to superior vertices (the black-to-white gradient reflects decreasing values of z-coordinates from inferior to superior areas, the black arrow indicates the sampling direction along the same axis). The average distance between finger

activation peaks was used to define the inferior and superior sampling borders. Different colors on the schematic drawing of the hand indicate different finger representations on the cortical surface. (B) qT1 values of one example participant sampled from inferior to superior vertices at 3 different layers (from top to bottom row: outer, middle, inner). Black lines represent local k-point mean values calculated over a sliding window of length k (5% of all data points) across neighboring vertices, light gray values represent individual data points. (C) Layer-dependent mean gradients (=mean of central differences between two neighboring sampling points) of qT1 values (in ms) and QSM values (in ppm, nQSM = negative, pQSM = positive, aQSM = absolute) were tested against zero. White dots represent the group mean. Black boxes represent the interquartile range. Whiskers are drawn within the standard error of the mean. Trends above Bonferroni-corrected threshold of p=0.016 (correcting for 3 tests per variable) are marked by a T. Potential outliers are represented by black dots.

Absence of Low-Myelin Borders between Finger Representations in S1

Next, we targeted our first research question on the presence or absence of low-myelin borders between finger representations in human S1, by comparing qT1 values sampled from the functional peak (highest t-value) of each finger representation with qT1 values sampled from the functional border between neighboring finger representations. The shortest path was estimated using the surface-based Dijkstra-algorithm (see **Figure 4A**), which is analogous to the way low-myelin borders between the hand and the face were detected (Kuehn et al., 2017a). We calculated layer-specific Bayesian probabilities (Bayes factors) as a relative measure of similarity for all neighboring finger pairs (D1-D2, D2-D3, D3-D4, D4-D5). Our results revealed that the alternative hypothesis (significant difference in myelin values between peak and border) was predicted a maximum 0.39 times better than the null hypothesis (no difference in myelin values between peak and border) in any layer (see **Table 2**, **Figure 4C**, **Figure 4D**). This provides evidence in favor of the null hypothesis of no difference, indicating an absence of low-myelin borders between finger representations in human S1.

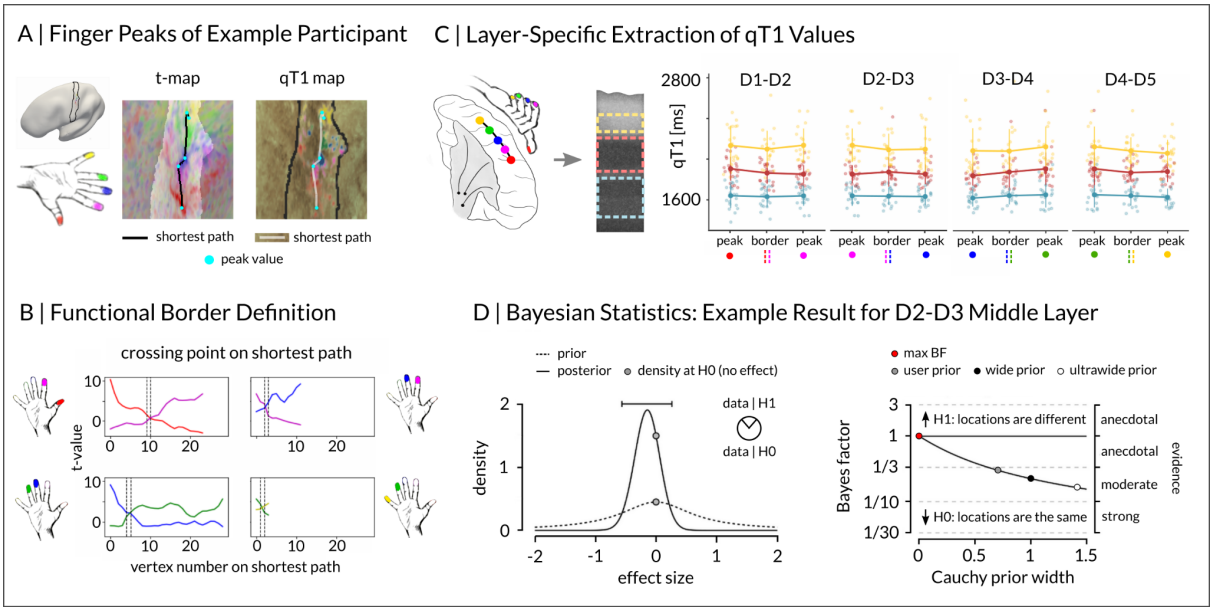

Figure 4. Absence of low-myelin borders between finger representations in human S1. (A) Locations of finger peak values (cyan dots) and estimated shortest paths between finger peaks (based on Dijkstra algorithm, solid black line in t-map, solid white line in qT1 map) within left S1 (light area in t-map, solid black line in qT1 map) are shown together with mapped t-values (five contrasts for five fingers, e.g. D1 (red) and qT1 values (darker areas reflect lower qT1 values, i.e. higher myelin content). (B) Locations of functional borders between fingers were defined as the vertex on the shortest paths where the t-value function of neighboring finger representations were equal (= crossing point, dashed black lines). From these vertices, qT1 values were sampled. Sampling of peak values is shown in (A). (C) qT1 values were sampled from finger peak and border locations (see (A) and (B)) in each layer (yellow: outer, red: middle, light blue: inner) resulting in 12 comparisons. Colored dots represent individual data, group means are plotted in bold. Whiskers represent the SEM. (D) Example of Bayesian Statistics. A Bayesian paired-sample t-test was calculated to test the peak-to-boder difference in qT1 between D2 and D3 in the middle layer. Prior distributions are shown as dashed lines, posterior distributions are shown as solid lines. Gray dots indicate the height of the curves (density) at the null hypothesis (H0). A Bayes factor of 1 or greater represents evidence in favor of the alternative hypothesis (H1), and a Bayes factor below 1 represents evidence in favor of the H0. The higher dot on the posterior distribution indicates that the Bayes factor supports the H0 (locations, i.e. peak and border, are the same).

		Peak		Border				
Layer	Condition	Mean qT1	SEM	Mean qT1	SEM	n	BF	error %
outer	D1-D2	2135.83	33.23	2099.25	40.42	20	0.34	0.019
	D2-D3	2117.55	32.35	2092.36	35.54	20	0.29	0.021
	D3-D4	2117.42	37.24	2094.50	49.70	19	0.27	0.016
	D4-D5	2105.28	21.12	2097.06	30.00	20	0.24	0.022
middle	D1-D2	1878.93	18.98	1863.54	23.51	20	0.39	0.016
	D2-D3	1852.47	18.23	1873.83	32.18	20	0.30	0.020
	D3-D4	1886.25	26.77	1889.12	35.00	19	0.24	0.016
	D4-D5	1906.63	23.59	1883.19	19.94	20	0.32	0.020
inner	D1-D2	1640.13	22.58	1630.30	23.09	20	0.30	0.020
	D2-D3	1635.73	18.32	1635.86	19.16	20	0.23	0.021
	D3-D4	1648.42	20.37	1656.81	20.03	19	0.26	0.016
	D4-D5	1652.61	21.06	1655.72	22.00	20	0.24	0.022

Table 2. Descriptives and Bayesian statistics of between-finger low-myelin border analysis. Shown are Bayesian paired-sample t-tests and Bayes factors (BF) as a relative measure of similarity of qT1 values for all finger pairs (D1-D2, D2-D3, D3-D4, D4-D5) at each layer (outer, middle inner). A Bayes factor of 1 or greater represents evidence in favor of the alternative hypothesis (significant difference between finger peak and border), and a Bayes factor below 1 represents evidence in favor of the null hypothesis (no difference between finger peak and border). The errors associated with the Bayes factor are given in %. Mean qT1 values and standard error of the mean (SEM) are given in milliseconds. qT1 values were sampled from finger peak (mean across two neighboring fingers) and border locations.

Also when exploring individual qT1 maps of the middle layer visually (where low-myelin borders should be located, Kuehn et al., 2017a), no systematic pattern of low-myelin borders separating functional finger representations could be detected (see **Figure 4-figure supplement 1**). But, as expected, low-myelin borders were clearly visible between the hand and the face areas (see **Figure 5**).

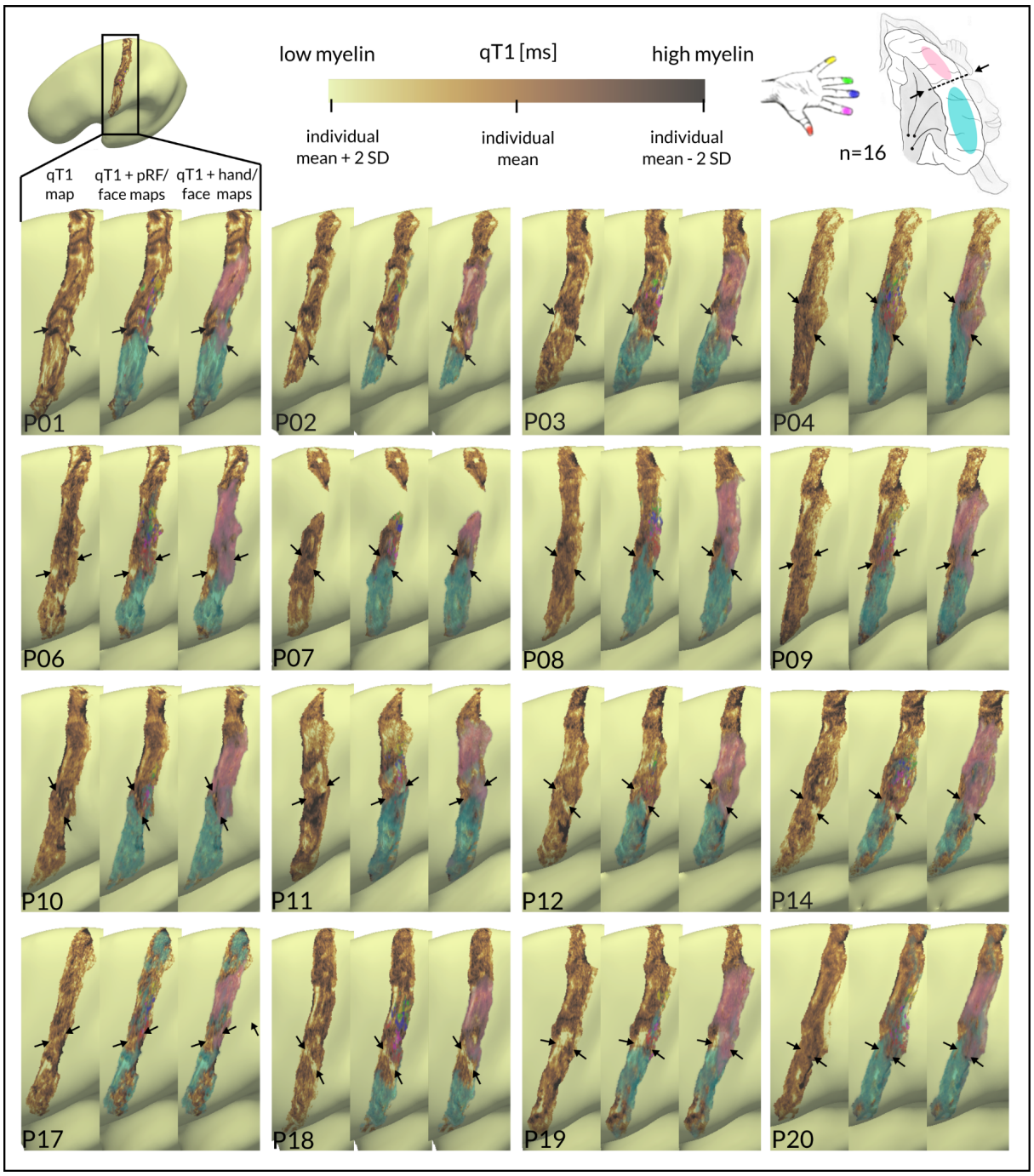

Figure 5. Individual qT1 maps of S1 show low-myelin borders between the face and hand areas. Cortical qT1 values extracted from the middle layer of left S1 (contralateral to where stimulation was applied or to where movement was carried out) are shown together with pRF center location maps of individual fingers (red: thumb, magenta: index finger, blue: middle finger, green: ring finger, yellow: little finger), functional face activation maps (clusters of highest t-values ($p<0.01$) colored in cyan) and functional hand activation maps (clusters of highest t-values ($p<0.01$) colored in light pink). Black arrows indicate low-myelin borders between face and hand representations in S1. qT1 values are given in milliseconds (ms), value ranges are thresholded individually within the mean +/- 2 standard deviations (SD). Areas of high myelin content (lower qT1 values) are colored in dark brown, while areas of low myelin content (higher qT1 values) are colored in olive green.

Non-Topographic 3D Structural Architecture of S1 Hand Area

To answer our second research question (i.e., whether finger representations differ in their 3D microstructural profiles), we compared the 3D microstructural profiles between individual finger representations using an ANOVA with the factors finger (D1, D2, D3, D4, D5) and layer (outer, middle, inner). For qT1 values, the analysis revealed a significant main effect of layer ($F(1.24,23.51)=466.84$, $p=7.6^{-18}$, $\eta^2=0.82$) with inner layers being more myelinated (showing lower qT1 values) than middle layers (inner: 1658.25 ± 6.35 (M ± SEM), middle: 1883.79 ± 7.13, $t(19)=28.89$, $p=3.7^{-17}$, $r=0.99$), and middle layers being more myelinated than outer layers (outer: 2105.19 ± 11.79; $t(19)=-14.58$, $p=9.0^{-12}$, $r=0.96$; $W=0$, $p=1.9^{-6}$), reflecting the intracortical myelin gradient described above. However, there was neither a significant main effect of finger ($F(4,76)=1.54$, $p=0.2$, $\eta^2=0.01$) nor a significant interaction effect between layer and finger ($F(3.92,74.53)=0.83$, $p=0.51$, $\eta^2=0.004$, see **Figure 6**).

The same ANOVA computed on pQSM values also showed a significant main effect of layer ($F(1.28,20.51)=4.89$, $p=0.03$, $\eta^2=0.05$), here driven by middle layers (likely encompassing the input layer IV) showing higher pQSM values (more iron) than inner layers (likely encompassing layers V and VI; middle: 0.010 ± 5.8^{-4}, inner: 0.009 ± 5.0^{-4}; $t(16)=3.84$, $p=0.001$, $r=0.69$; $W=14$, $p=0.002$). Similar as for qT1 values, there was neither a significant main effect of finger ($F(1.89,30.2)=0.32$, $p=0.71$, $\eta^2=0.01$) nor a significant interaction between layer and finger ($F(2.81,44.88)=1.52$, $p=0.23$, $\eta^2=0.02$). The same ANOVA on aQSM values also showed a significant main effect of layer ($F(1.46,24.86)=16.38$, $p=1.1^{-4}$, $\eta^2=0.12$), here driven by outer layers showing more mineralization than middle layers (outer: 0.011 ± 4.2^{-4}, middle: 0.010 ± 5.0^{-4}; $t(17)=3.09$, $p=0.007$, $r=0.60$; $W=22$, $p=0.004$), and middle layers showing more mineralization than inner layers (inner: 0.009 ± 4.0^{-4}; $t(17)=3.71$, $p=0.002$, $r=0.67$; $W=19$, $p=0.002$). However, similar as for qT1 and pQSM, there was neither a significant main effect of finger ($F(2.44,41.54)=0.21$, $p=0.85$, $\eta^2=0.004$) nor a significant interaction effect ($F(3.59,61.04)=1.07$, $p=0.38$, $\eta^2=0.02$).

Finally, the same ANOVA on nQSM values again showed a main effect of layer ($F(2,30)=45.72$, $p=7.8^{-10}$, $\eta^2=0.26$), here driven by more negative nQSM values (higher diamagnetic contrast) in outer compared to middle layers (outer: -0.012 ± 5.4^{-4}, middle: -0.008 ± 4.7^{-4}; $t(15)=-9.37$, $p=1.2^{-7}$, $r=0.92$; $W=0$, $p=3.1^{-5}$). Again, there was no significant main effect of finger ($F(4,60)=0.97$, $p=0.43$, $\eta^2=0.02$), but a significant interaction between layer and finger ($F(3.94,59.06)=2.78$, $p=0.04$, $\eta^2=0.05$). This interaction was driven by more negative nQSM values (higher diamagnetic tissue contrast) in the inner layers for D1

compared to D4 (D1: -0.010 ± 6.7^{-4}, D4: -0.007 ± 4.2^{-4}, t(15)=-3.82, p=0.002, r=0.70) and for D1 compared to D5 (D5: -0.007 ± 5.3^{-4}, t(15)=-3.13, p=0.007, r=0.63).

Together, except for more diamagnetic tissue contrast in D1 compared to D4 and D5 in inner layers of S1, our results show that the 3D structural architecture with respect to myelin, iron and mineralization does not significantly differ between the representations of single fingers in S1 (see **Figure 6-figure supplement 1** for analyses on outlier-removed data and equally-spaced layers).

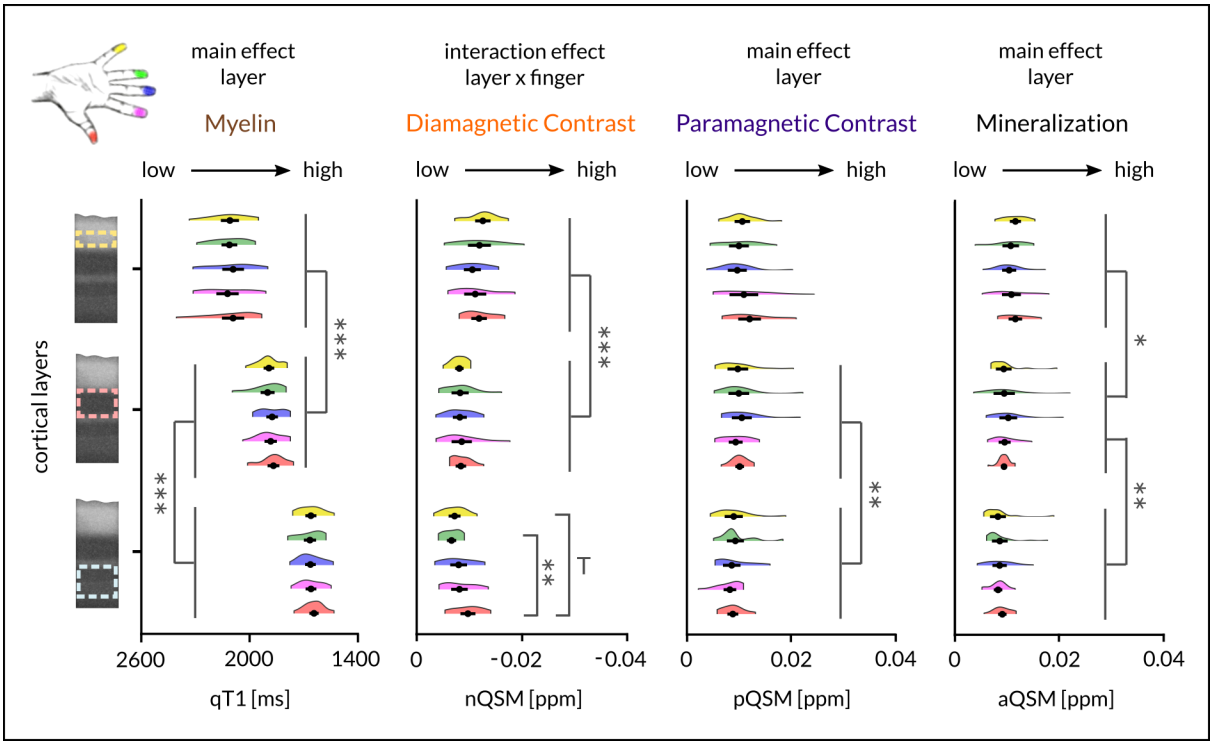

Figure 6. Non-topographic 3D structural architecture of the S1 hand area. Two-way repeated-measures ANOVAs (layer x finger) on qT1 (n=20), nQSM (n=16), pQSM (n=17) and aQSM (n=18) revealed significant differences in myelin content, diamagnetic contrast (e.g., calcium), paramagnetic contrast (iron) and mineralization content between layers (* p<0.025 , ** p<0.005, *** p<0.0005). Trends above Bonferroni-corrected threshold of p=0.005 correcting for 10 tests per layer to follow up a significant interaction are marked by a T. Fingers are shown in different colors: red: D1, magenta: D2, blue: D3, green: D4, yellow: D5. Except for more nQSM (higher diamagnetic contrast) in D1 compared to D4 and D5 in inner layers (light blue dotted line), the 3D structural architecture with respect to myelin, paramagnetic contrast (iron) and mineralization does not significantly differ between the representations of single fingers in S1. Myelin staining was remodeled according to Dinse et al. (2015) and shows anatomically-relevant layers (dotted lines, creme: outer layer, light pink: middle layer, light blue: inner layer) as reference. Black dots represent the mean, whiskers are drawn within the standard error of the mean.

In addition, we compared intracortical meta parameters (i.e., skewness, kurtosis; in classical parcellation often used to differentiate between brain areas; e.g. Dinse et al., 2015) between finger representations. Using one-way repeated-measures ANOVAs with factor finger (D1, D2, D3, D4, D5), there were no significant differences (see **Figure 7B,** for exact statistical results see **Figure 7-figure supplement 1**).

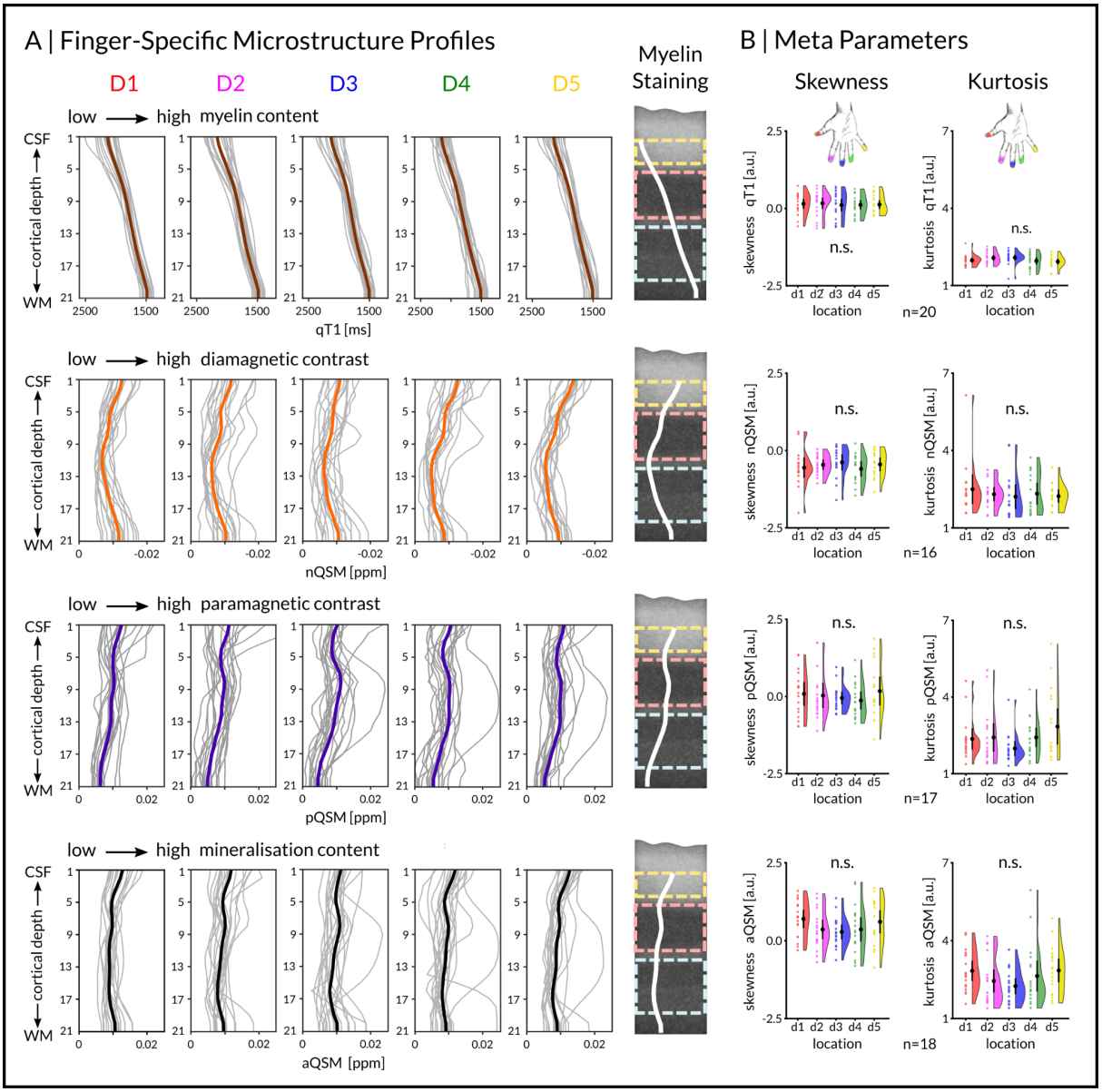

Figure 7. Finger-specific 3D microstructure profiles and intracortical meta parameters do not differ between S1 finger representations. (A) Quantitative T1 (qT1, reflecting myelin, n=20, group mean plotted in brown), negative QSM (nQSM, n=16, reflecting diamagnetic tissue contrast/calcium, group mean plotted in orange), positive QSM (pQSM, reflecting paramagnetic tissue contrast/iron, n=17, group mean plotted in purple) and absolute QSM (aQSM, reflecting mineralization, n=18, group mean plotted in black) sampled at 21 different cortical depths. Depth 1 is located closest to CSF, depth 21 is located closest to WM. Profiles of thumb (D1), index finger (D2), middle finger (D3), ring finger (D4), and little finger (D5) are shown. Myelin staining was

remodeled according to Dinse et al. (2015) and shows anatomically-relevant cortical compartments (creme: outer layer, light pink: middle layer, light blue: inner layer) and average microstructure profiles across fingers (white lines) as reference. (B) Comparison of intracortical meta parameters between fingers using one-way repeated measures ANOVAs with within-subjects factor finger (red: D1, magenta: D2, blue: D3, green: D4, yellow: D5) revealed no significant (n.s.) differences in skewness and kurtosis between fingers. Values are given in arbitrary units (a.u.). Black dots represent the group mean. Whiskers (black lines) are drawn within the standard error of the mean. Colored dots represent individual data.

Phenotyping the Human S1 Hand Area

Above, we have shown that the 3D structural architecture of the human S1 hand area is homogenous as neither low-myelin borders nor systematic structural differences between finger representations were detected. Finally, we target our third research question to see if interindividual variation in this non-topographic microstructural profile explains interindividual variation in functional and behavioral readouts. This analysis can be regarded as a first step to answer the much broader research question of how the 3D microstructure of a given cortical field can be 'phenotyped'. Given the relatively low sample size and the high number of tests, we used a correlation matrix to provide an overview over possible relationships. This correlation matrix includes structural variables (layer-specific qT1, nQSM, pQSM, aQSM values), functional map features (cortical responsivity (%-signal change), precision (pRF size), functional connectivity (Eigenvector centrality)) and tactile behavior (along the same dimensions of responsivity (tactile detection), precision (2-point discrimination, finger discrimination) as well as sensorimotor integration (feedback task) for both D2 only (note that some behavioral tests were done on D2 only) and the whole hand area (note that other tactile tests involved the whole hand; see **Figure 8** and **Figure 8-figure supplement 1** for exact statistical results).

With respect to structure-structure correlations, we observe highest intra-layer relationships in the outer layer (rho > 0.74), lower intra-layer relationships in the middle layer, and overall lowest intra-layer relationships in the inner layer of the S1 hand area. Note that correlation coefficients only report the strength of a relationship (i.e., absent: rho < 0.1, weak: rho = 0.1, moderate: rho = 0.3, strong: rho = 0.5; Cohen, 1988), but do not compare different hypotheses against each other.

Correlation coefficients between structural and fMRI metrics, i.e. %-signal change and pRF sizes, are mostly negative in all three layers, indicating that lower qT1/QSM-based substance concentration has a tendency to reflect higher %-signal change and lower pRF

sizes (i.e., more precise pRFs). For functional connectivity, however, the pattern was reversed, and higher qT1/QSM-based substance concentration, particularly in the middle and inner layers, has a tendency to reflect higher network centrality (i.e. Eigenvector centrality computed based on rectified linear unit correlation of resting-state signal fluctuations (EC-RLC), Lohmann et al., 2018).

Correlation coefficients between structural and behavioral markers indicate that lower QSM-based substance concentration in the outer layer but higher QSM-based substance concentration in the inner layer relate to better 2-point discrimination thresholds. For finger discrimination (i.e., correctly identifying D2 when touched at the 50% threshold; Liu et al., 2021), this pattern was reversed. For tactile detection and sensorimotor integration, the relationship to structural markers was generally absent or low.

Together, these exploratory analyses show that structure-structure relationships follow a layer-specific pattern with co-localization of paramagnetic and diamagnetic substances particularly in superficial layers. While structure-structure correlations in superficial and middle layers were high, the relationships between structure and fMRI, and between structure and behavior were generally lower, except for the relationship between structure and EC-RLC. Interestingly, correlation coefficients between structural and most behavioral and fMRI markers (except for finger discrimination and EC-RLC) were negative, i.e., higher qT1/QSM-based substance concentration has a tendency to relate to ‘worse behavior’ or lower fMRI responsivity/precision.

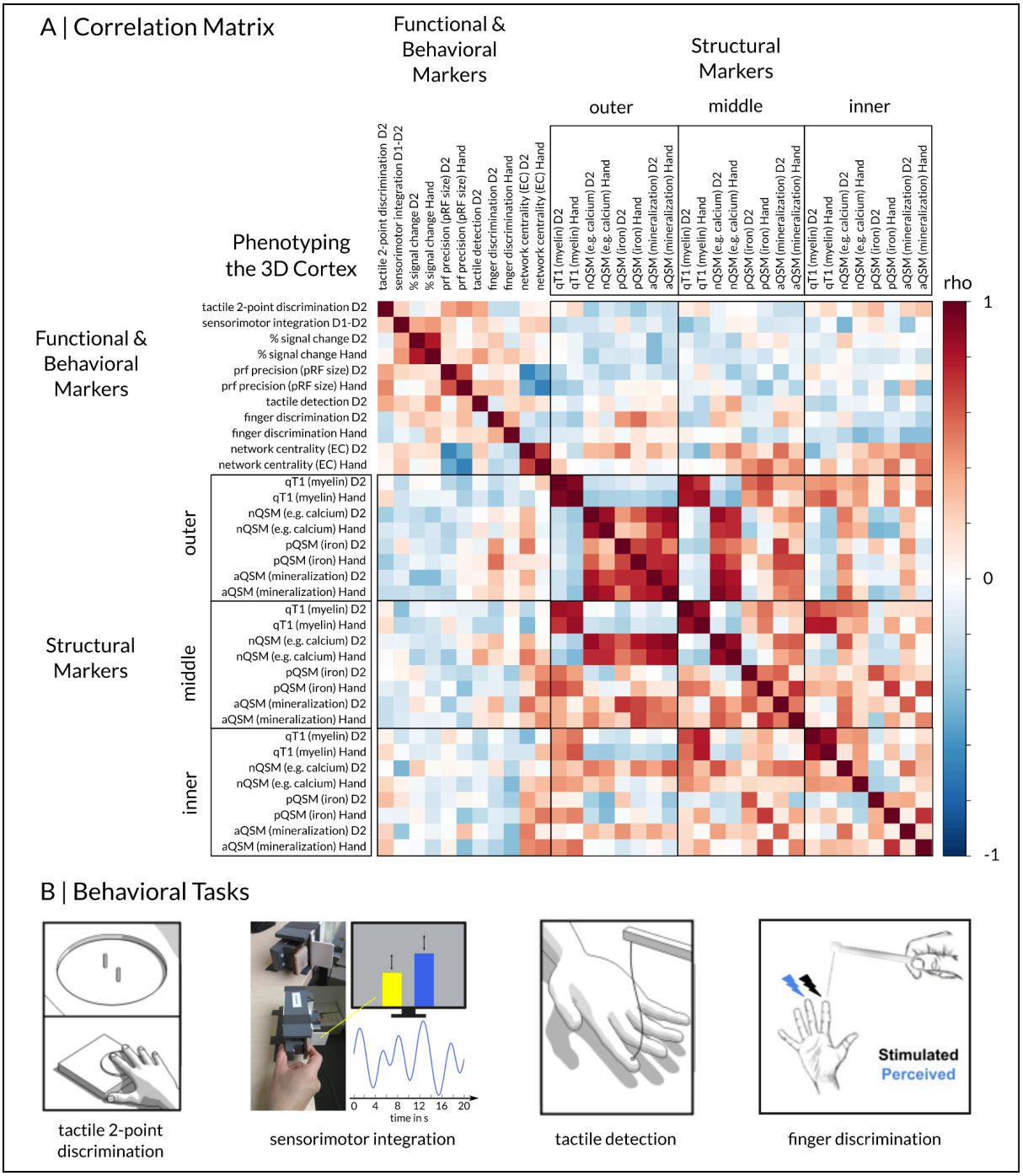

Figure 8. Phenotyping the Human S1 Hand Area. (A) Functional and behavioral correlates of 3D structural features (qT1: myelin, nQSM: e.g. calcium, pQSM: iron, aQSM: mineralization). Top row: structure-function/structure-behavior correlations, other rows: structure-structure correlations. Correlation coefficients are given as Spearman's rho. Correlations were calculated for the hand (full finger map) and the D2 (index finger), because most tasks were performed for D2 only (tactile detection, 2-point discrimination), or involved D2 (finger discrimination, sensorimotor integration). Positive correlations are shown in red, negative correlations are shown in blue. To ensure that higher values indicate better performance, higher precision or more myelin, the values of tactile detection, 2-point discrimination, pRF sizes and qT1 were reversed, nQSM values were taken as absolute values. (B) Summary of behavioral tasks that were included in the phenotyping analyses.

Topographic 3D Structural Architecture of S1 Hand-Face Area

To demonstrate that the methods used here are sensitive to capture topographic differences, we carried out a control analysis comparing layer-specific qT1, pQSM, nQSM and aQSM between the functionally-localized face and the hand areas. A two-way repeated measures ANOVA on qT1 values with factors layer (inner, middle, outer) and body part (face, hand) revealed a significant interaction effect ($F(1.37,20.55)=15.72$, $p=2.7^{-4}$, $\eta^2=0.02$). qT1-based myelin content was lower in the hand compared to the face area in inner (face: 1601.19 ± 12.36, hand: 1638.62 ± 11.84, $t(15)=2.91$, $p=0.011$, $r=0.6$) and outer layers (face: 2067.11 ± 21.31, hand: 2097.74 ± 20.39, $t(15)=2.22$, $p=0.042$, $r=0.5$, see **Figure 9**).The same ANOVA computed on pQSM values revealed a significant main effect of body part ($F(1,13)=10.92$, $p=0.006$, $\eta^2=0.12$). pQSM-based iron content was highest in the hand area (hand: 0.011 ± 4.3^{-4}, face: 0.009 ± 3.6^{-4}). For aQSM values there was also a significant main effect of body part ($F(1,13)=10.92$, $p=0.006$, $\eta^2=0.13$), showing highest mineralization content in the hand area (hand: 0.010 ± 3.5^{-4}, face: 0.009 ± 3.3^{-4}); whereas for nQSM values there was no significant difference between body parts.

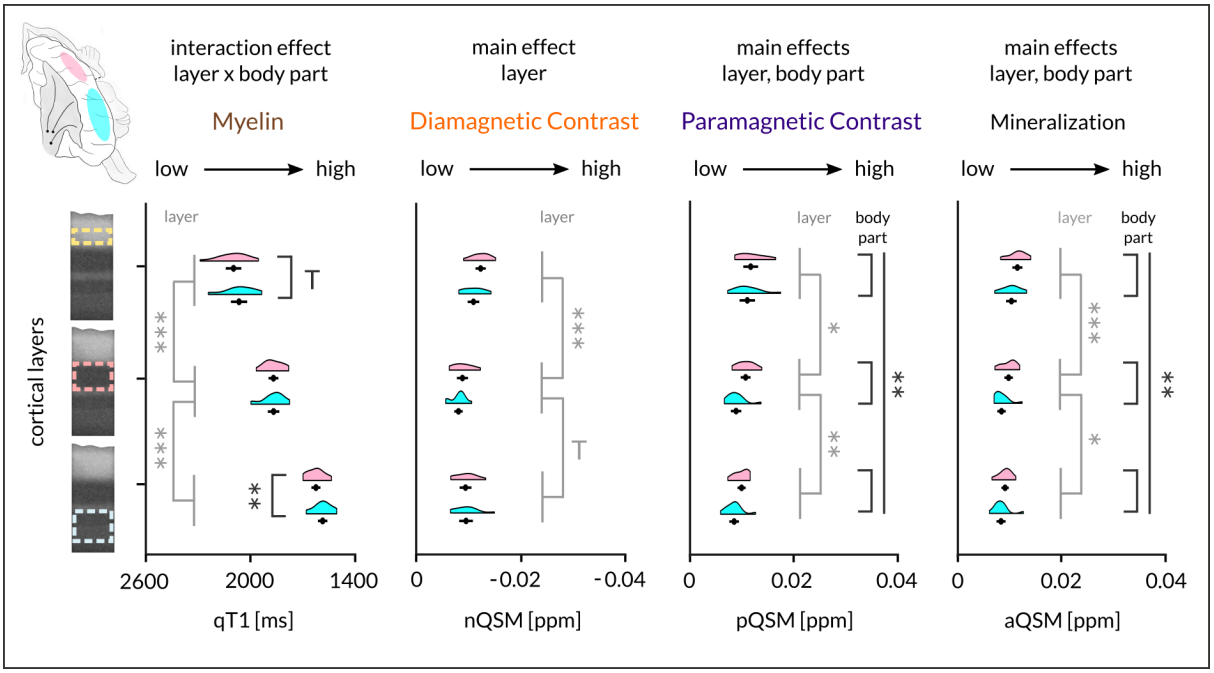

Figure 9. Topographic 3D structural architecture of the S1 face-hand area. Two-way repeated-measures ANOVAs (layer x body part) on qT1 (n=16), nQSM (n=14), pQSM (n=14) and aQSM (n=14) revealed significant differences in myelin content, diamagnetic contrast (e.g., calcium), paramagnetic contrast (iron) and mineralization content between layers (significance statement colored in light gray, $p < 0.025$ *, $p < 0.017$ **, $p < 0.001$ ***). Trends above Bonferroni-corrected threshold of $p=0.017$ correcting for 3 tests per layer to follow up a significant interaction are marked by a T. Body parts are shown in different colors (light pink: hand, cyan: face). Except for nQSM (diamagnetic contrast), the 3D structural architecture, with respect to myelin, paramagnetic

contrast (iron) and mineralization, differs significantly between the representations of the hand and face in S1 (significance statement colored in dark gray). Myelin staining was remodeled according to Dinse et al. (2015) and shows anatomically-relevant layers (dotted lines, creme: outer layer, light pink: middle layer, light blue: inner layer). Black dots represent the mean, whiskers are drawn within the standard error of the mean.

Together, except for nQSM, our results show that the 3D structural architecture, with respect to myelin, iron and mineralization, significantly differs between the representations of the face and the hand in S1, whereas, as explained above, the 3D structural architecture between single finger representations does not significantly differ.

Discussion

We here use sub-millimeter quantitative MRI proxies for myelin, iron and mineralization to describe the 3D structural architecture of the human S1 hand area in relation to its functional organization and behavioral readouts. We show that precise intra-cortical tissue contrasts can be extracted from a group of younger adults, which are replicable across individuals, and can be used to define anatomically-relevant layer compartments. While low-myelin borders were visible between the representations of the hand and the face, such borders were absent between individual finger representations. Similarly, while the 3D structural architecture significantly differed between the representations of the hand and the face, it did not differ between individual finger representations or along the inferior-to-superior axis (except for the deep layers of the thumb). Phenotyping the 3D profile indicated a tendency of lower qT1/QSM-based substance concentration relating to higher responsivity and precision. Conversely, higher qT1/QSM-based substance concentration was related to higher network centrality, confirming previous results. Taken together, our data show that the 3D structural architecture of the human S1 hand area is homogenous and essentially non-topographic, although functional finger representations are distinct and discontinuous. This difference compared to the structural architecture of the S1 hand area in monkeys and to the hand-face area in humans reveals novel mechanistic insights into the flexibility of finger representations and cortical plasticity.

As expected from histological studies (e.g. Vogt, 1919) and *in vivo ex vivo* validation work (Stüber et al., 2014, Dinse et al., 2015), we showed an intra-cortical myelin gradient with increasing myelin content (decreasing qT1 values) from superficial to deep cortical depth. By relating our data to remodeled *in vivo ex vivo* validated S1 data (Dinse et al., 2015), we extracted three anatomically-relevant cortical compartments that contained estimates for S1 layers IV and V/VI. This approach is novel, because in previous work, data of only few participants were investigated extensively (e.g., Alkemade et al., 2022, Huber et al., 2020), or layers were defined arbitrarily by dividing the cortex into equally-spaced compartments (Kuehn et al., 2017a, Tardiff et al., 2015). While our layer definition was based on cortical myelination (i.e., qT1 values), the pQSM and nQSM data also fit to this compartmentalization scheme, since the two iron peaks coincide with the expected locations of the Baillarger bands in anatomical layers IV and V, and the U-shaped nQSM profile shows a small plateau where we expected layer IV to be located. This scheme was therefore used to describe the S1 3D architecture in more detail.

With respect to low-myelin borders, we do not find evidence for such borders between finger representations in S1, which seems to differentiate humans from monkeys (Jain, Catania & Kaas, 1998, Qi & Kaas, 2004). While functional topographic borders suggest high selectivity, an absence of structural borders may introduce flexibility to finger (re-)alignment. In human S1, more overlap between neighboring finger representations and reduced cortical distances between index and middle finger representations have for example been described in older adults (Liu et al., 2021). In older rats, upper limb and whisker representations, that are separated by septa, remain intact (Spengler et al., 1995, Coq & Xerri, 2000, Godde et al., 2002, David-Jürgens et al., 2008). Indeed, structural borders have in the past been related to reducing plasticity (Sereno, 2005). However, 'double-thumb' representations or differences in finger alignment order between participants (Liu et al., 2021) could be described by a more flexible architecture. In reelin-deficient mice, where the primary visual cortex is intra-cortically disorganized, visual cortical plasticity is enhanced (Pielecka-Fortuna et al., 2015). Thus, an absence of sharp structural borders (both vertically and horizontally) may allow more distributed information (Muret et al., 2022), facilitating cortical flexibility.

An absence of low-myelin borders between S1 finger representations also has conceptual implications. Although single fingers are functionally distinct units that partially receive distinct input, our findings suggest that all fingers are represented as one structural unit. Low-myelin borders in the cortex may therefore separate cortical representations that are nearby in the cortex but distant in the real word, as previously shown for the hand and face (Glasser et al., 2016, Kuehn et al., 2017a, Northall et al., 2022). When cortical representations are nearby in the cortex and also nearby in the real word, such as for individual fingers, GABA-ergic functional inhibition may allow their differentiation (Kuehn et al., 2014). Low-myelin borders may therefore reflect real world features, rather than only mediating inhibition. This also explains why structural and functional parcellation does not always align (Zhi et al., 2002), and relates to the concept that local stability and global reorganization of finger representations are driven by distributed, rather than finger-specific, processing underlying the topographic map (Wesselink et al., 2022). An absence of low-myelin borders between S1 finger representations is therefore in line with recent observations, and suggests that the hand area is encoded as an integrated unit, shaped in close relation to real world features such as external spatial location (Haggard et al., 2006).

We further show no significant differences in the 3D structural profiles between individual fingers (except for the thumb), even though our data could be used to detect such

differences between the hand and the face. In human M1, large-scale body part representations are not only separated by low-myelin borders, but also differ in their microstructural profiles (Northall et al., 2022). This, together with our data, indicates that low-myelin borders and 3D structural differences coincide, providing evidence that large-scale body part representations can be regarded as distinct cortical fields (Sereno et al., 2022). In addition, our data suggests that small-scale body parts are structurally more integrated than large-scale body parts. This may be of functional relevance, since sensorimotor behaviors are more likely to involve a whole hand or foot compared to single fingers or toes, indicating that small-scale body parts require less integrated coordination with the rest of the body.

The exception to the rule is the thumb, which shows higher diamagnetic contrast in deeper layers compared to the ring and the little finger. This may be explained by its special role for tool use. In a recent study in macaque monkeys, cortical organization was suggested to reflect hand use with respect to an opposable thumb (Lazar et al., 2022). Most neurons in the S1 thumb representation specifically respond to tactile stimulation of the thumb, but not to tactile stimulation of other fingers, and interconnect only sparsely to other digit representations. The thumb representation may thus act as an independent module processing selective information, whereas information content is more distributed between other fingers.

When phenotyping the human S1 hand area, higher paramagnetic and diamagnetic substance concentration is related to higher network centrality. This is in line with previous research showing that areas of higher myelin content (such as S1) also present with higher resting-state connectivity (Glasser et al., 2016, Huntenburg et al., 2017, Kuehn et al., 2017a), which supports microstructural wiring rules. Here, we add that this relationship is particularly strong in inner and middle layers, indicating that myelin and iron are specifically linked to intracortical and cortical-subcortical loops.

One novel result is that lower qT1/QSM-based substance concentration has a tendency to relate to better performance (except for network centrality and finger discrimination). This contradicts established concepts such as “more myelin = higher structural integrity = better processing” and raises the question as to in which circumstances increased cortical iron or myelin may be dysfunctional. Studies in animals (reviewed in Peters, 2009) showed a link between increased cortical myelin in older age and the production of redundant myelin

sheaths. It is argued that the myelin is overproduced, therefore weakening its original purpose. Similarly, investigating remyelination after induced damage mimicking natural myelin loss in mice, researchers found that myelin is not only rebuilt in expected locations, but also outside of target regions, which is assumed to be dysfunctional (Snaidero et al., 2020). One hypothesis is that the qT1 and/or QSM-signal may have partly captured this 'off-target' remyelination, which would explain its relation to worse behavior. Future research investigating qT1 and QSM stability in humans over time may resolve this question.

Addressing study limitations, it should be noted that absence of evidence should not be equated with evidence of absence. Although positive controls (S1 face-hand area) are provided, it still remains possible that potential low-myelin borders between finger representations could not be detected with the given methodology. In addition, the sample size of this study is relatively low. Consequently, type I and type II errors are more difficult to reduce (Sullivan et al., 2016). However, since the recruitment process took multiple years (starting in 2016), it was not feasible to investigate higher participant numbers. Also note that the sample size is, however, relatively high compared to previous 7T-MRI studies (e.g. Kuehn et al., 2017, Huber et al., 2020). To reduce type I error, we corrected for multiple comparisons and restricted the number of statistical tests to the minimum number needed. To reduce type II errors, we show statistical trends (i.e., $p > 0.05$ and < 0.1, see **Figures 3, 6** and **9**). Critically, the method used here has been demonstrated to be sensitive to detect low-myelin borders in S1 in even smaller samples (Kuehn et al., 2017a).

Taken together, our data provide the first comprehensive *in vivo* description of the 3D structural architecture of the human S1 hand area and show it to be non-topographic. This distinguishes the human S1 hand area from the "barrel field" of rodents and the hand area of monkeys, which may be related to topographic organizational differences between species. The specific homogeneous representation of the S1 hand area in humans suggests that there are less structural limitations to cortical plasticity and reorganization. Studying the microstructure of the cortex is therefore critical to fully understand topographic change in the course of aging, learning, or disease. These new insights encourage future studies to incorporate the dimension of cortical layers into new testable models, and consider structural limitations of plasticity for intervention methods.

Methods

Participants

24 healthy volunteers underwent 7T MRI and behavioral experiments of tactile and motor finger performance. Due to severe head motion during scanning, 4 participants were excluded from the study, leaving a total of 20 participants for analysis (10 females, mean age = 25 +/- 3 years). According to the Edinburgh handedness questionnaire (Oldfield, 1971), all participants were right-handed (laterality index ranging from +33 to +100, M = 82 +/- 21 SD). Chronic illness, central acting medications and MRI contraindications (e.g., active implants, non-removable metallic objects, claustrophobia, tinnitus or hearing impairments, consumption of alcohol/drugs) were a priori exclusion criteria.

Participants showed no anomalies of sensory perception (e.g., numbness, tingling sensations) or motor movement (e.g., reduced motor control, restricted finger movement), and no diagnoses of diabetes or hypertension. No professional musicians participated, given evidence of enlarged cortical hand representations and superior tactile perception in string and piano players (Elbert et al., 1995; Ragert et al., 2004; Schwenkreis et al., 2007). Finally, none of the participants showed signs of cognitive impairments as indicated by the 'Montreal Cognitive Assessment' (Nasreddine et al., 2005; M = 29 +/- 1 SD, scores ranging from 26 to 30). Participants were recruited from the database of the DZNE Magdeburg. All participants gave their written informed consent and were paid for their participation. The study was approved by the Ethics committee of the Otto-von-Guericke University Magdeburg. fMRI data were partly published in a previous study (Liu et al., 2021).

General Procedure

Participants took part in 4 appointments: (i) Structural MRI session, (ii) Functional MRI session, (iii) Behavioural session 1 (tactile 2-point discrimination (2PD), tactile detection and sensorimotor behaviour), (iiii) Behavioural session 2 (finger discrimination) (see **Figure 1** for experimental design and analysis pipeline of MRI data).

MRI Assessment

MR sequences

MRI data were acquired at a 7-Tesla MAGNETOM scanner (Siemens Healthcare, Erlangen, Germany) equipped with a 32 Channel Nova Medical head coil. First, MP2RAGE (Marques et al., 2010) whole brain images were acquired at 0.7 mm isotropic resolution (240 sagittal

slices, field-of view read = 224 mm, repetition time = 4800 ms, echo time =2.01 ms, inversion time TI1/TI2 = 900/2750 ms, flip angle = 5 ◦ /3 ◦ , bandwidth = 250 Hz/Px, GRAPPA 2), and MP2RAGE part brain images (covering the sensorimotor cortex) were acquired at 0.5 mm isotropic resolution (208 transversal slices, field-of-view read = 224 mm, repetition time = 4800 ms, echo time = 2.62 ms, inversion time TI1/TI2 = 900/2750 ms, flip angle = 5 ◦ /3 ◦ , bandwidth = 250 Hz/Px, GRAPPA 2, phase oversampling = 0%, slice oversampling = 7.7%). We additionally acquired uncombined susceptibility-weighted imaging (SWI, Haacke at al., 2004) data with part brain coverage of sensorimotor cortex at 0.5 mm isotropic resolution using a 3D gradient-echo pulse sequence (208 transversal slices, field-of-view read = 192 mm, repetition time = 22 ms, echo time = 9.00 ms, flip angle =10◦, bandwidth = 160 Hz/Px, GRAPPA 2, phase oversampling = 0%, slice oversampling = 7.7%). The total scanning time was approximately 60 minutes. Prior to collecting functional data, shimming was performed and two EPIs with opposite phase-encoding (PE) polarity were acquired. Functional EPI sequences (gradient-echo) were acquired using the following parameters: voxel resolution of 1 mm isotropic, field-of-view read: 192 mm, repetition time = 2000 ms, echo time = 22 ms, GRAPPA 4, interleaved acquisition, 36 slices.

fMRI task

Five independently-controlled MR-compatible piezoelectric stimulators (Quaerosys, http://www.quaerosys.com) were used to stimulate the five fingertips of the right hand of the participants in the scanner (Schweisfurth et al., 2015, 2014, 2011). A stimulator was attached to each fingertip of the right hand, using a custom-built, metal-free applicator to adjust to individual hand and finger sizes. Each stimulator consisted of 8 individually-controlled pins arranged in a 2x4 matrix, covering 2.5x9 mm^2 of skin (see **Figure 1**). Vibrotactile stimulation was applied at a frequency of 16 Hz (Schweizer et al., 2008), and stimulation intensity was adjusted individually for each participant and each finger to 2.5 times the individual tactile detection thresholds. To minimize adaptation-related variation in map activity between participants, two randomly selected pins were raised once at a time, yielding 16 pin combinations per second (Schweisfurth et al., 2015, 2014, 2011).

Participants first underwent two phase-encoded protocols (runs 1 and 2 of the experiment), which included 2 runs of 20 cycles each. Each cycle lasted 25.6 seconds where each fingertip was stimulated 20 times for 5.12 seconds. Stimulation was applied either in a forward (D1->D5) or in a reverse order (D5->D1, see **Figure 1**). Half of the participants started with the forward-run, while the other half started with the reverse-run. One run

comprised 256 scans (512 seconds for a TR of 2 seconds), and lasted for 8 minutes and 31 seconds. Participants were instructed to covertly count short, randomly distributed pauses during the tactile stimulation (duration 180 ms). We used the same number of gaps per finger, resulting in 15 gaps in total per run. Participants then underwent the blocked-design protocol (runs 3 and 4 of the experiment), which included 6 conditions: Stimulation to D1, D2, D3, D4, D5, and a rest condition with no stimulation. The same task instructions and stimulation protocol as described for the phase-encoded paradigm was used, although fingers were stimulated in a pseudo-random way, where fingers were not stimulated more than two times in a row. Between two subsequent stimulations, there was a 2 seconds pause (in 70% of the trials), or a 6 seconds pause (in 30% of the trials), which was counterbalanced across fingers. Each finger was stimulated 10 times. One run comprised 208 scans, and lasted for 6.56 minutes. The blocked-design run was repeated twice. Subsequently, two runs were recorded where a one-TR stimulation of all five fingers was followed by a 11-TR resting phase without any stimulation. The sequence was repeated 10 times for both runs. Finally, resting-state data were acquired in a 5-minute scan. Participants were asked to look at a centrally placed fixation cross, and to think about nothing in particular. All together, functional measurements took approximately 40 minutes.

Physiological Data Recording

During the fMRI scans, physiological data were acquired. To measure the pulse, a pulse oximeter (NONIN Pulse Oxymeter 8600-FO) was clipped to the index finger of the participant's left hand (where no stimulator was attached) and participants wore a breathing belt to capture respiration. An in-house developed setup was used to digitally record and analyze the physiological data (hardware employing National Instruments USB 6008 module with pressure sensor Honeywell 40PC001B1A). The sampling frequency was set to 200 Hz.

MRI Analyses

Structural Data Processing

Data Preparation

Structural data quality was evaluated by two independent raters and data showing severe artifacts (i.e., of n=3 participants) were excluded. We only used data showing mild truncation artifacts (not affecting S1), or no artifacts at all. Quantitative susceptibility maps (QSM) were reconstructed from coil-uncombined SWI magnitude and phase images using the Bayesian multi-scale dipole inversion (MSDI) algorithm (Acosta-Cabronero et al., 2018) implemented

in the software qsmbox (version v3, freely available for download: https://gitlab.com/acostaj/QSMbox, Acosta-Cabronero et al., 2018) written for Matlab (R2017b, The MathWorks Inc., Natick, MA, 2017). Structural MP2RAGE and QSM images were then processed using JIST (Lucas et al., 2010) and CBS Tools (Bazin et al, 2014) as plug-ins for the research application MIPAV (McAuliffe et al, 2001).

Registration

First, the qT1 and QSM slab images were co-registered to the up-sampled (0.7 to 0.5 mm isotropic) whole brain qT1 image. To precisely register the qT1 slab image onto the resampled whole brain qT1 image, we combined linear transformation (MIPAV v7.3.0, McAuliffe et al., 2001, Optimized Automated Registration Algorithm: 6 degrees of freedom, cost function of correlation ratio) and non-linear deformation (ANTs version 1.9.x-Linux, Avants et al., 2011, embedded in cbstools wrapper Embedded Syn, cost function of cross correlation) in one single step, using nearest neighbor interpolation. For registration of the QSM slab image, we applied a combination of rigid and affine automated registration using the software ITK-SNAP (version 3.6.0, freely available for download at www.itksnap.org). The registration quality of resulting qT1 and QSM slab images were evaluated by two independent raters. The generated registration matrix for the qT1 slab image was then applied to the UNI and INV2 images.

Segmentation

qT1 slab and whole-brain images were fused using a weighted combination of images, resulting in one whole-brain structural image with improved resolution in the sensorimotor cortex. Using the merged images, brain surrounding tissues (i.e., skull and dura mater) were removed and resulting brain masks were manually refined (using both the qT1 and UNI images) to ensure that all non-brain matter was removed from S1. The cortex was then segmented using the UNI image as input for the TOADS algorithm (Bazin & Pham, 2007) to estimate each voxel's tissue membership probability. The results were used as input for the CRUISE algorithm (Han et al., 2004) to estimate the inner and outer gray matter (GM) borders (i.e. to the WM and CSF, respectively). The resulting level set images (surfaces in Cartesian space using a level set framework, Sethian, 1999) were optimized to precisely match S1, by thresholding the maximum values of the inner and outer level set images to -2.8 and -0.2, respectively.

Layering and Surface Mapping

The level set images were then used to generate individual surfaces for cortical mapping. Intra-cortical qT1 and QSM values, used as proxies for myelin (Stueber, 2014) and mineralization (Acosta-Cabronero et al., 2016, Acosta-Cabronero et al., 2018, Betts et al., 2016), respectively, were estimated in reference to individual cortical folding patterns using the validated equivolume model (Waehnert et al., 2014, Waehnert et al., 2016). The cortical sheath was initially divided into 21 level set surfaces where we sampled qT1 and QSM values to derive cortical depth-dependent profiles. Finally, the extracted values were mapped onto the individual's inflated cortical surface (method of closest point, Tosun et al., 2014). Please note, for cortical depth-dependent mapping of quantitative values, we used the non-merged high-resolution qT1 and QSM slab data to ensure high data quality. We extracted three different parameter maps from the QSM data (negative QSM (nQSM), positive QSM (pQSM), absolute QSM (aQSM)) to estimate information on different underlying tissue properties (diamagnetic tissue contrast for nQSM, paramagnetic tissue contrast for pQSM, level of mineralization for aQSM).

Extracted cortical depth-dependent profiles were further averaged into fewer compartments following two different approaches: 1) To ensure comparability of our results to previous data, the 3 most superficial and the 2 deepest profiles were removed to reduce partial volume effects (Tardif et al., 2015), before the remaining 16 profiles were averaged into 4 equally-spaced cortical depth compartments (in the following referred to as 'equally-spaced layers': superficial, outer-middle, inner-middle, deep). 2) We followed recent *ex vivo in vivo* validation studies in S1 that allow definition of anatomically-relevant cortical compartments from ultra-high resolution MRI data (Dinse et al., 2015). We used previously validated myelin profiles of Brodman area (BA) 3b (Dinse et al., 2015) to identify cortical compartments based on averaged qT1 profiles (at the group level) by plotting histological data as well as modeled and *in vivo* MRI data of Dinse et al. (2015) in reference to our *in vivo* MRI data (for detailed description see **Figure 1-figure supplement 1**). Calculating minima and maxima of the first derivative of the initial qT1 profile (including 21 compartments) allowed us to extract 3 data-driven cortical-depth compartments that are anatomically relevant: After removing the 2 deepest layers (where qT1 stabilized and a plateau was reached, see **Figure 1-figure supplement 1**), the remaining 19 compartments were averaged into an inner (8 deepest layers), middle (7 layers) and outer (4 most superficial layers) cortical-depth compartment, where based on Dinse et al., 2015, the input layer IV is located in the middle compartment and the deep layers V/VI are located in the inner compartment. In the main text, analyses are

shown for 3 layer compartments, results of identical analyses for 4 layer compartments are provided as supplemental material.

Anatomical Definition of S1

We manually generated subject-specific S1 masks of the left hemisphere based on anatomical landmarks in the qT1 images (Geyer, Schleicher, & Zilles, 1999; Yousry et al., 1997), using the software ITK-SNAP (version 3.6.0). Masks were drawn from the crown of the postcentral gyrus to the fundus of the central sulcus, covering the posterior wall of the postcentral gyrus (Geyer, Schleicher, & Zilles, 1997). Only those slices were masked in which the knob-like (axial slices) or the hook-like shape (sagittal slices) of the motor hand area was visible. Adjustments were made where required until the S1 surface mask presented homogenous and without holes.

Functional Data Processing

Distortion correction of opposite polarity EPIs was performed using a point spread function (PSF) mapping (In et al., 2016). To account for differences in the amount of spatial information between the opposite PE EPIs, a weighted combination of the two distortion-corrected images was applied to generate the final, corrected image. The EPI-images of the functional scans were motion corrected to time point = 0. PSF mapping was applied to the motion-corrected images to perform geometrically accurate image reconstruction. Functional time series were slice time corrected to account for differences in image acquisition time between slices using SPM8 (Statistical Parametric Mapping, Wellcome Department of Imaging Neuroscience, University College London, London, UK). Slice-time corrected functional data resulting from phase-encoded protocols were concatenated.

Registration of Functional Data

First, task-dependent functional time series were automatically registered to the resting-state functional time series (ITK-SNAP version 3.6.0, rigid transformation, cross correlation similarity metric, interpolation method: Nearest Neighbor). Second, resting-state time series were manually registered to the MP2RAGE qT1 image (ITK-SNAP version 3.6.0, non-rigid transformation, 9 degrees of freedom). Resulting registration matrices were applied to the corresponding functional parameter maps (i.e., t-maps, pRF estimates, EC maps) in a single step (using ANTs, version 2.1.0, nearest neighbor interpolation). The inverse of the resulting registration matrices were used to transform individual ROI masks from structural into

functional data space (Advanced Normalization Tools (ANTs), version 2.1.0, nearest neighbor interpolation), allowing us to perform ROI analysis on non-smoothed functional data.

GLM Analysis of Blocked Design Data

We used the general linear model (GLM) as implemented in SPM8 to individually calculate fixed-effects models on the 1st level of the two blocked-design runs (runs 3 and 4 of the experiment, see **Figure 1**). Because each finger was treated individually and independently, BOLD activation driven by each finger's tactile stimulation was included in the quantification as an independent measure (Kuehn et al., 2018a, Ann Stringer et al., 2014). Each session was modeled with five regressors of interest (stimulation to D1, D2, D3, D4, D5) and allowed the computation of five linear contrast estimates: Touch to D1, D2, D3, D4, and D5 (e.g. the contrast [-1 4 -1 -1 -1] for touch to D2).

Bayesian pRF Modeling

Population receptive field (pRF) modeling was performed on the phase-encoded fMRI data following the same procedure as introduced by Liu et al. (2021), incorporating the SPM-based BayespRF Toolbox (freely available for download from https://github.com/pzeidman/BayespRF) written for Matlab (SPM12 and Matlab R2017b). We performed a two-stage analysis: First, a 1st level GLM analysis was conducted using SPM12 to prepare the data for pRF modeling by reducing the number of voxel time courses. At this stage, the task regressors were defined. Five regressors were constructed, corresponding to the five fingers of the right hand. Only time-series data that passed a significance threshold of $p<.05$ uncorrected were taken forward for pRF modeling (Zeidman et al., 2018, Puckett et al., 2020). pRF modeling was restricted to the S1 region (using our S1 masks) to reduce the computing time considerably (note that pRF modeling of one participant takes around 24 hours for the given input data, i.e., it would take several days to compute all data of one participant). pRF modeling was then conducted on a voxel-by-voxel basis to optimize the fit between an estimated waveform and the empirically measured BOLD-response, by modifying the size and position of the pRF model. We thresholded the posterior model probability at >0.95 (Liu et al., 2021; Puckett et al., 2020; Zeidman et al., 2018). To define the somatosensory space, the dimensions of the 2D matrix were limited to +/- 12.5. Finally, pRF modeling was performed on the inferior-superior dimension (x-dimension) of topographic alignment. The minimal pRF size was restricted to 1/10th of the sensory space occupied by a single fingertip, whereas the maximum pRF size was restricted to the equivalence of all five

fingers (i.e., 25 units; Liu et al., 2021). A Gaussian pRF profile was chosen as the response function for the pRF analysis (code available for download at https://gitlab.com/pengliu1120/bayesian-prf-modelling.git). The model was characterized by a normal, excitatory distribution with pRF center location (x) and pRF width (i.e., σ, the standard deviation of the Gaussian profile) as parameter estimates. The extracted distance parameter was used to define the digit ROIs (locations of activated voxels for each finger) whereas the extracted width parameter was used as pRF size estimate of activated voxels. Because the stimulus space was one-dimensional, only pRF distance (i.e. center location) and pRF size parameters were further analyzed in surface space.

Mean Response Amplitude

To calculate mean response amplitudes, statistical analyses were conducted on the averaged individual time series of the averaged forward- and reversed-order runs from the phase-encoded paradigm (Kuehn et al., 2018a, Liu et al., 2021), using the program Fourier implemented in csurf (http://www.cogsci.ucsd.edu/~sereno/.tmp/dist/csurf). Discrete Fourier transformations were performed on the time course of each 3D voxel, before calculating phase and significance of the periodic activation. Cycles of 20 stimulations were used as input frequencies. Frequencies below 0.005 Hz (known to be dominated by movement artifacts) were excluded, while higher frequencies up to the Nyquist limit (1/2 the sampling rate) were included. For display, a vector was generated whose amplitude was the square root of the F-ratio calculated by comparing the signal amplitude at the stimulus frequency to the signal amplitude at other noise frequencies, and whose angle was the stimulus phase. To estimate mean response amplitudes of the five finger ROIs (in %), we estimated the discrete Fourier transform response amplitude (hypotenuse given real and imaginary values) for each voxel, within each finger's pRF center location area (see above). This value was multiplied by two to account for positive and negative frequencies, again multiplied by two to estimate peak-to-peak values, divided by the number of time points over which averaging was performed (to normalize the discrete Fourier transform amplitude), and divided by the average brightness of the functional data set (excluding air). Finally, the value was multiplied by 100 to estimate percentage response amplitude (Kuehn et al., 2018a, Liu et al., 2021).

Localizing Single Fingers in S1

Resulting pRF center location maps were used to locate the hand area and single finger representations in S1. We applied a "winner-takes-it-all" approach to the pRF center location maps to ensure vertices are sampled only once (i.e. excluding overlapping map areas

between finger representations). Vertices of overlapping areas (introduced by splitting pRF maps into five single finger maps and mapping single finger maps onto the inflated surfaces) were exclusively assigned to one area by taking the highest variance (explained by the pRF model) as criterion. The hand area was defined by combining the five fingers to one larger ROI.

Localizing the Face-Hand Area in S1

A sub-sample (n=16 participants) also underwent functional 7T MRI (gradient-echo EPI sequence of 1.5 mm isotropic resolution with part-brain coverage of M1/S1) while carrying out motor movements of the tongue and the fingers to locate the face-hand area in M1 (Northall et al., 2022). Here, we used these movement-related data to locate the face-hand area in S1. After the functional data was manually registered, based on anatomical landmarks, to the MP2RAGE qT1 image (ITK-SNAP version 3.6.0, non-rigid transformation, 9 degrees of freedom), we estimated functional activation maps of tongue and finger movements (peak clusters of t-values, thresholded at $p < 0.01$ with a minimum cluster size of k=3) using the GLM as implemented in SPM12 (first-level analysis based on contrast estimates for each body parts, for details see Northall et al., 2022). A “winner-takes-it-all” approach was applied to the resulting localizers to ensure vertices are sampled only once (i.e., excluding overlapping map areas between body part representations).

Resting-State Data Analysis

Resting-state functional data were corrected for pulse- and respiration-induced noise. To prepare the physiological data for noise correction and to remove acquisition artifacts, we used the open-source Python-based software ‘PhysioNoise’ (Kelley et al., 2008). Resulting respiratory and cardiac phase data were then used to correct the resting-state time series for pulse- and respiration-induced noise by performing RETROspective Image CORrection (RETROICOR) (Glover et al., 2000) on a slice-by-slice basis (Birn et al., 2006). Residuals were taken as cleaned data to regress out motion-related noise parameters (extracted from the raw data) using the program vresiduals implemented in LIPSIA (freely available for download at: github.com/lipsia-fmri/lipsia, Lohmann et al., 2001). The resulting data were high-pass filtered at 0.01 Hz (allowing frequencies faster than 0.01 Hz to pass) and smoothed (Gaussian kernel with a FWHM of 2 mm) using the program vpreprocess implemented in LIPSIA. For n = 2 participants, physiological data were not successfully recorded due to loosening the pulse oximeter and/or breathing belt during scanning, which interrupted successful data sampling. For n = 5 participants, severe motion artifacts were

detected in the resting-state data. Therefore, resting-state analyses are presented for n=13 participants only.

Eigenvector Centrality (EC) Mapping

EC maps were calculated in native space to generate maps of functional network hubs using the program vecm, implemented in LIPSIA (Lohmann et al., 2001). Thereby, the method of rectified linear unit correlation (RLC, Lohmann et al., 2018) was applied, which is suitable for high-resolution fMRI data. The resulting EC maps were registered to the participant's individual anatomical space to perform analyses restricted to the left S1 hand area.

Surface Mapping of Functional Parameters

Registered functional parameters were mapped onto the individual surfaces in anatomical space using the method of closest point (Surface Mesh Mapping algorithm), and S1 masks were applied. To minimize the effect of superficial veins on BOLD signal change, the most superficial 20% of cortical values were disregarded and the mean value of the remaining layers (20–100% cortical depth) were used to perform statistical analyses.

Extracting Microstructural Profiles

We sampled qT1, nQSM, pQSM and aQSM values perpendicular to the cortical sheet at 21 different cortical depths from the pRF center locations of the five fingers, and from the face-hand area in S1. Within subjects, extracted values were averaged across vertices (resulting in one value per location/body part and depth). We then calculated the first and the second derivative of resulting qT1 vectors using the gradient function implemented in MATLAB (R2017b). Minima and Maxima of the first derivative were estimated by finding the zero locations in the second derivative.

Extraction of Inferior-to-superior Structural Gradients

Vertex-wise extraction of layer-specific qT1, nQSM, pQSM and aQSM values from the S1 region (see section Anatomical Definition of S1) was performed for all participants individually using MATLAB (R2017b). The extracted data was sorted along the z-dimension (inferior-to-superior axis) and averaged across the x- and y-dimension (dimension reduction from 3D to 1D) resulting in vectors of sorted quantitative values (from inferior to superior). The inferior border of the extracted vectors was defined as the z-coordinate of the vertex that lies the average peak-to-peak distance (number of vertices between finger activation peaks along inferior-to-superior axis) inferior from the D1 activation peak (maximum *t*-value,

generated based on blocked design data), whereas the superior border was defined as the z-coordinate of the vertex that lies the average peak-to-peak distance superior from the D5 activation peak (maximum *t*-value generated based on blocked design data). Finally, inferior-to-superior qT1, nQSM, pQSM and aQSM gradients were calculated as central differences between two neighboring sampling points of sorted vectors.

Septa Analysis

To investigate whether between-finger septa also exist in human S1, a surface-based mapping approach combining functional and structural data was used (Kuehn et al., 2017a). Layer-specific qT1 values and functional activity (*t*-values generated based on blocked design data) were sampled along predefined paths between neighboring finger representations. In particular, we compared qT1 values extracted from peak locations (location of maximum t-value) with qT1 values extracted from border locations (intersection points of t-value vectors sampled along the shortest path between peak locations of neighboring S1 finger representations, similar approach to Kuehn et al., 2017a). We used the Dijkstra algorithm as implemented in Pyvista for Python (Sullivan & Kaszynski, 2019) to calculate the shortest path between peak locations of neighboring S1 finger representations (D1-D2, D2-D3, D3-D4, D4-D5; as well as between D2-D1 and D1-D3 in one case where locations of D1 and D2 finger maps were reversed). All in all, qT1 values of n=20 younger adults were sampled from 9 different locations (5 peaks, 4 borders) at 3 different cortical depths (inner, middle, outer).

Statistics of MRI and fMRI Data

Statistical analyses were computed in R (version 3.4.4, R Core Team, 2018). All sample distributions were analyzed for outliers using boxplot methods and tested for normality using Shapiro-Wilk's test. In case of non-normal data, non-parametric or robust tests are reported. For all tests, the significance level was set to p = .05. Bonferroni-corrected significance levels were applied for multiple testing to correct for family-wise error accumulation. Pearson's correlation coefficient r was calculated as an effect size estimator for Student t-tests and Wilcoxon signed-rank tests. We applied Cohen's criteria of 0.3 and 0.5 for a medium and large effect, respectively. Eta-squared (η^2) was calculated as an effect size estimator for ANOVAs.

To test for the existence of inferior-to-superior structural gradients within the human S1 hand area, extracted layer-specific qT1, nQSM, pQSM and aQSM gradients were averaged across

neighboring sampling points (along the z-dimension), separately for each participant. Resulting mean gradients were compared against zero using two-tailed one-sample t-tests against zero. Non-parametric Wilcoxon signed rank tests were calculated where conditions of the parametric one-sample t-test were violated.

To compare skewness and kurtosis of microstructure profiles between fingers, one-way repeated-measures ANOVAs on qT1, nQSM, pQSM and aQSM with finger (D1, D2, D3, D4, D5) as within-subjects factor were computed given normality. In case of non-normal data, we report robust repeated-measures ANOVAs based on 20%-trimmed means which were performed using the rmanova function from the WRS2 package (version 1.1-3, Mair and Wilcox, 2018) in R.

To test for layer-specific differences in qT1, nQSM, pQSM and aQSM between finger representations, we calculated two-way repeated-measures ANOVAs with layer (inner, middle, outer) and location (D1, D2, D3, D4, D5) as within-subjects factors. In case of sphericity violations, Greenhouse-Geisser-corrected results (when violations to sphericity were large, i.e. epsilon < .75) or Huynd-Feldt-corrected results (when violations to sphericity were small, i.e. epsilon >= .75) were computed. Post-hoc tests were performed as two-tailed paired-samples tests. Non-parametric Wilcoxon signed rank tests were additionally calculated where conditions of the parametric one-sample t-test were violated. For sample distributions containing extreme outliers (values above the third quartile plus 3 times the interquartile range or values below the first quartile minus 3 times the interquartile range), two-way repeated-measures ANOVAs were computed both with and without extreme outliers included. Please note that in order to offer data that can more easily be compared to previous studies, we repeated the analyses using the equally-spaced layer definition. These results are reported in the supplemental material, whereas in the main text, we report the results of the anatomically-relevant compartments.

To test for layer-specific differences in qT1, nQSM, pQSM and aQSM between the face and the hand representation, we calculated two-way repeated-measures ANOVAs with layer (inner, middle, outer) and body part (face, hand) as within-subjects factors using the same correction methods and post-hoc tests as described above.

To investigate whether between-finger septa also exist in human S1, we performed layer-wise comparisons on peak-to-border differences of qT1 values by applying Bayesian

paired-samples t-tests (resulting in 12 tests given 4 different peak-to-border conditions (D1-D2, D2-D3, D3-D4, D4-D5) and 3 different cortical depths). For this purpose, qT1 values were averaged across neighboring finger representations for each peak-to-border condition (i.e., D1-D2 average, D2-D3 average, D3-D4 average, D4-D5 average). The JASP software package (version 0.8.1.2, JASP Team, 2017) was used to calculate Bayesian paired-samples t-tests with location (peak, border) as within-subjects factor. We used a Bayes factor favoring the alternative hypothesis. The default Cauchy-scaled prior of 0.707 was selected instead of modeling the expected effect size. However, we simulated the effect of the prior on the Bayes factor for a wider range of prior width to estimate how robust the conclusions were to the chosen prior.

To investigate whether functional features were systematically related to layer-specific structural features in S1 finger maps, percent signal change, pRF size and ECM values averaged both within the D2 finger map and across the full finger map, were correlated with qT1, nQSM, pQSM and aQSM values of the corresponding maps. Correlation analyses were computed as rank correlations using Spearman's rho correlation coefficient to account for non-normal data. Uncorrected correlation coefficients are reported.

Behavioral Assessment

Tactile Detection Task

Tactile detection of touch to the surface of the fingertip was assessed using fine hair stimuli. We used a subset (0.008 g, 0.02 g, 0.04 g, 0.07 g, 0.16 g, 0.4 g, 0.6 g, 1.0 g, 1.4 g, 2.0 g, 4.0 g, 6.0 g) of standardized tactile monofilaments (Semmes-Weinstein monofilaments; Baseline, Fabrication Enterprises Inc., White Plains, NY, USA) to apply different mechanical forces to the skin surface of finger tips (see **Figure 1**). Stimuli were manually applied to a predefined skin area (circle with a diameter of approximately 2 mm), touching the skin surface at an angle of approximately 90 degree, for one second (Mücke et al., 2014). Stimulus application was guided by auditory instructions via headphones which were controlled by the Psychophysics Toolbox extensions (Brainard, 1997; Kleiner et al., 2007; Pelli, 1997) in MATLAB (R2017b). All participants sat in front of a screen that signaled the beginning and ending of stimulus intervals and listened to white noise via headphones. The right hand, with the palm facing upwards, was fixated on a small pillow behind a paper wall so that participants were neither able to see their own hand nor the experimenter.

In a two-alternative forced choice paradigm, participants chose one of two possible time intervals that contained the stimulation, where the stimulation was randomly applied in the first or second interval (Gescheider et al., 1996; Thornbury & Mistretta, 1981). Application of tactile monofilaments followed a 3-down/1-up staircase approach with two interleaved staircases, one starting at a weight of 0.02 gram and the other starting at a weight of 0.4 gram. The stimulus weight was increased by one step after each error, and decreased by one step after every three correct responses (not necessarily in a row), until stable performance was reached (Gescheider et al., 1996). This procedure was separately applied for each of the two staircases, but presentation of staircase steps followed an interleaved manner (Cornsweet, 1962). The experiment was finished when for the last 30 trials the variation in stimulus intensity from the mean (standard deviation) was 1 step or less (Gescheider et al., 1996), or when the maximum number of 100 trials was reached. The participant‘s tactile detection threshold was defined as the mean stimulus intensity across reversal points (change of response from correct to incorrect or incorrect to correct) within the period of stable performance (Thornbury & Mistretta, 1981), which was in this case defined as the last 30 trials. Individual within-finger detection thresholds were estimated for the five fingers of the right hand, taking approximately 12 min per finger.

Finger Discrimination Task

Again, Semmes Weinstein monofilaments were used to apply tactile stimulation to the five fingers of the right hand, targeting the same stimulation sites as described for the tactile detection task (marked area at finger tip, see above), with applied forces matching the respective tactile detection thresholds previously measured. In a five-alternative-forced-choice design, tactile stimulation (lasting 1 second) was applied to one of five possible fingertips. Participants were asked to name the finger where they felt the touch. Answers were given verbally within a limited response interval (lasting 7 seconds). In case participants perceived no touch (note that tactile stimulation was applied at individual detection thresholds and was therefore expected to be perceived only in approximately 50% of the cases), they were motivated to guess. Each fingertip was stimulated 20 times, using unique pseudo-randomized sequences (with fingertips being stimulated not more than two times in a row).

2-Point Discrimination Task (2PDT)

To assess tactile discrimination performance of the participant’s right D2 (similar to Kalisch et al., 2008; Kuehn et al., 2017b; Pleger et al., 2016), we used a 2PDT. Stimulation was applied

by two rounded pins (diameter = 0.4 mm) simultaneously touching the surface of the fingertip. A custom-made, fully automatic stimulation device moved the pins up and down, controlled by the commercial software package Presentation (version 16.5, Neurobehavioral Systems, Inc., Albany, CA, USA). The amplitude of pin movement was adjusted to the individual detection threshold (as assessed before in the finger detection paradigm), but was at least set to 1.2 mm. Spacing between pins ranged from 0.7 to 2.8 mm (in steps of 0.3 mm). Additionally, a single pin was included as control condition. Pin spacing was vertically adjusted by rotating a disc containing all possible pin spacing conditions (n = 9). In a two-alternative forced-choice paradigm, pin spacing conditions were pseudo-randomly presented. Participants were asked to indicate whether they perceived one or two single pins touching their fingertip. They were instructed to give the answer “two pins felt” only if they were certain. The 1 pin condition served as a control. The right D2 was fixated on the stimulator, and the hand was covered by a white box during the task to prevent effects caused by seeing the stimulated finger (Cardini et al., 2011, Cardiniet al., 2012). Each task block included 90 trials (10 repetitions per pin condition). To prevent order effects, unique sequences of pin spacing conditions were used per participant and task block. All participants completed two task blocks. Intertrial intervals were pseudo-randomized and varied between 1 to 5 seconds (in steps of 1 second) to avoid fixed clock cycles gating reactions.

Precision Grip Task

Sensorimotor grip force and precision grip performance were assessed with a custom made pressure sensor that was held between the D1 and D2 of the right hand, adjusted to individual strength (see **Figure 1**) (Vieluf et al., 2013). Reference forces that were to be matched in the precision grip paradigm ranged from 5 % to 25 % of the individual maximum grip force to avoid muscle fatigue (Voelcker-Rehage & Alberts, 2005). In the precision grip paradigm, participants solved a visuo-motor matching task (Gryga et al., 2012, Vieluf et al., 2013) demanding them to continuously adjust the grip force applied to the pressure sensor. Applied forces were digitally sampled at a frequency of 100 Hz and projected on screen at a refresh rate of 60 Hz. The task was fully automated and controlled by the software package Presentation (version 16.5, Neurobehavioral Systems, Inc., Albany, CA, USA).

To test the ability of grip force adjustment, each task repetition contained a unique pseudo-randomized sequence of 10 position changes at five different amplitudes (5%, 10%, 15%, 20%, 25% of maximum grip force) leading to a mean frequency of 0.25 Hz. After a

period of task familiarization (Gryga et al., 2012, Voelcker-Rehage & Alberts, 2005), all participants were asked to perform the task for a total duration of 20 seconds. One task block contained 15 task repetitions divided by inter-task intervals of 10 seconds each, leading to a total duration of about 8 minutes per task block. All participants performed two task blocks that were separated by a 5-minute resting period. After each task repetition, participants received feedback about their individual performance level (mean position difference in pixel) on screen. Participants were asked to place their right arm on the table and put fingers D1 and D2 on the pressure sensitive key. As a behavioral outcome measure, we monitored the time (in seconds) the controllable bar was within a given percentage above (2.5%) and below (2.5%) the target line (upper edge of the reference bar) continuously throughout the experiment (Vieluf et al., 2013; Voelcker-Rehage & Alberts, 2005).

Behavioral Analyses

Tactile Detection Threshold

Individual tactile detection thresholds correspond to the mean stimulus intensity applied at reversal points of the last 30 trials. This means that only those trials were included in the calculation in which a response change (from correct to incorrect or incorrect to correct) occurred (Kalisch et al., 2008; Thornbury & Mistretta, 1981). Before averaging, stimulus intensities were transformed logarithmically on a 1/10th milligram scale (log 10 0.1mg), yielding approximately equal intervals between filaments. For further statistical analysis the log-transformed values were used. Lower values indicate higher tactile sensitivity to mechanical forces. Additionally, we estimated the skin indentation in mm based on the examined detection threshold. For this purpose, detection thresholds were taken as proxies of corresponding values in milliNewton (mN) that were provided by the manufacturer. Afterwards, the skin indentation δ was calculated according to the following equation which was derived from Wu, Dong, Smutz, and Rakheja (2003):

$$\delta = [(F/A)\ (1/b)\ ] * \bar{\delta}$$

F is the estimated force in Newton (N), A (= 0.2368 N) and b (= 2.0696) are material/structural constants and $\bar{\delta}$ (= 1.00 mm) is the reference indentation (Wu et al., 2003). Finally, the result (δ) was multiplied by 3 to get an indentation value clearly above threshold which was used to increase the amplitude of pin movement in the 2PD task. All calculations were performed in Matlab (R2017b).

Finger Discrimination Sensitivity

To extract the finger discrimination sensitivity (sensitivity of one finger being correctly discriminated from other fingers), we applied signal detection theory and calculated the d-prime as bias-free index of discrimination sensitivity by computing the amount of times a specific finger was touched and detected (hit), or was not touched but falsely detected (false alarm). Hits and false alarms were first converted to z-scores before subtracting false alarms from hits. D-primes were obtained for each finger separately.

2PD Threshold

2PD thresholds were calculated per participant and run. Answers “two pins felt” were fitted as percentages across ascending pin distances (0.7 - 2.8 mm). A binary logistic regression was used to fit the data using the glmfit function (iterative weighted least square algorithm to receive maximum-likelihood estimators) from the Statistics Toolbox implemented in MATLAB (R2017b). The 2PD threshold was taken from the pin distance where the 50 percent level crossed the fitted sigmoid curve (e.g. Kalisch et al., 2008; Kalisch et al., 2009; Kuehn et al., 2017; Pleger et al., 2001). Please note that lower values indicate higher spatial acuity.

Precision Grip Accuracy

For each participant, precision grip accuracy was taken as the time (in seconds) the upper edge of the controllable bar (sensitive to applied pressure) was within a 5% target range surrounding the upper edge of the moving target bar (2.5% below and above the upper edge of the target bar; Vieluf et al., 2013; Voelcker-Rehage and Alberts, 2005). The position difference of the edges was continuously monitored throughout the task and captured every 16.67 milliseconds. Values were then averaged for each task repetition leading to 30 averaged values per participant, reflecting the time within target range. Finally, the 30 values were averaged into one value for each participant. Higher values reflect higher precision grip accuracy.

Statistics of Behavioral Tasks

All sample distributions were analyzed for outliers using boxplot methods and tested for normality using Shapiro-Wilk’s test. Tactile detection thresholds of right D2 as well as finger discrimination sensitivity of right D2 and mean finger discrimination sensitivity across all fingers, 2PD sensitivity of right D2 (averaged across runs) and precision grip accuracy, involving both right D1 and right D2, were correlated with layer-specific qT1, nQSM, pQSM and aQSM values of corresponding finger representations. Correlation analyses were

performed using Spearman's rho correlation coefficient. Uncorrected results are reported. Please note that, before calculating correlations, the data was partly transformed (using the reciprocal of tactile discrimination thresholds, detection thresholds, pRF sizes and qT1 values, as well as absolute nQSM values), so that in the final correlation matrix, higher values always indicate better performance in behavior, higher precision, higher responsivity, and more connectivity in fMRI markers, as well as higher substance concentration in structural MRI markers.

Author Contributions

Conceptualization: E.K., J.D.

Methodology: J.D., E.K., A.F., G.L., O.S.

Formal Analysis: J.D., A.N., P.L., E.K., A.C.

Investigation: J.D., E.K.

Writing - original draft preparation: J.D.

Writing - review and editing: J.D., E.K., A.N., P.L., A.C., A.F., O.S., G.L., T.W.

Visualization: J.D.

Supervision: E.K.

Funding acquisition: E.K.

All authors contributed to the article and approved the submitted version.

Competing interests

No competing interests to declare.

Acknowledgments

This project was funded by the German Research Foundation (Deutsche Forschungsgemeinschaft, DFG) (KU 3711/2-1, project number: 423633679 and Project-ID 425899996 – SFB 1436). A.N. was funded by the Else Kröner Fresenius Stiftung: 2019-A03.

We would like to thank Lilith-Sophie Lange and Miriam Weber for their support in data collection, Jörg Stadler for helping with physiological data analysis, Pierre-Louis Bazin and Daniel Haenelt for giving advice on ultra high-resolution image processing and Nikolaus Kinder for his graphical support.

References

Acosta-Cabronero, J., Betts, M. J., Cardenas-Blanco, A., Yang, S., & Nestor, P. J. (2016). In Vivo MRI Mapping of Brain Iron Deposition across the Adult Lifespan. *The Journal of Neuroscience*, 36 (2), 364–74. https://doi.org/10.1523/JNEUROSCI.1907-15.2016

Acosta-Cabronero, J., Milovic, C., Mattern, H., Tejos, C., Speck, O., & Callaghan, M. F. (2018). A robust multi-scale approach to quantitative susceptibility mapping. *Neuroimage*, 183, 7-24. https://doi.org/10.1016/j.neuroimage.2018.07.065

Ann Stringer, E., Qiao, P. G., Friedman, R. M., Holroyd, L., Newton, A. T., Gore, J. C., & Min Chen, L. (2014). Distinct fine-scale fMRI activation patterns of contra-and ipsilateral somatosensory areas 3b and 1 in humans. *Human Brain Mapping*, *35* (9), 4841-4857. https://doi.org/10.1002%2Fhbm.22517

Avants, B. B., Tustison, N. J., Song, G., Cook, P. A., Klein, A., & Gee, J. C. (2011). A reproducible evaluation of ANTs similarity metric performance in brain image registration. *NeuroImage*, 54 (3), 2033–2044. https://doi.org/10.1016/j.neuroimage.2010.09.025

Bazin, P. L., & Pham, D. L. (2007). Topology-preserving tissue classification of magnetic resonance brain images. *IEEE Transactions on Medical Imaging*, *26* (4), 487-496. https://doi.org/10.1109/TMI.2007.893283

Bazin, P.-L., Weiss, M., Dinse, J., Schäfer, A., & Trampel, R. (2014). A computational framework for ultra-high resolution cortical segmentation at 7Tesla. *NeuroImage*, 93, 201–209. https://doi.org/10.1016/j.neuroimage.2013.03.077

Birn, R. M., Diamond, J. B., Smith, M. A., & Bandettini, P. A. (2006). Separating respiratory-variation-related fluctuations from neuronal-activity-related fluctuations in fMRI. *Neuroimage*, *31*(4), 1536-1548. https://doi.org/10.1016/j.neuroimage.2006.02.048

Blake, D. T., Byl, N. N., & Merzenich, M. M. (2002). Representation of the hand in the cerebral cortex. *Behavioural Brain Research*, *135* (1-2), 179-184. https://doi.org/10.1016/S0166-4328(02)00163-8

Brainard, D. H. (1997). The Psychophysics Toolbox. *Spatial Vision*, 10 (4), 433–6.

Cardini, F., Costantini, M., Galati, G., Romani, G. L., Làdavas, E., & Serino, A. (2011). Viewing One's Own Face Being Touched Modulates Tactile Perception: An fMRI Study. *Journal of Cognitive Neuroscience*, 23 (3), 503–513. https://doi.org/10.1162/jocn.2010.21484

Cardini, F., Longo, M. R., Driver, J., & Haggard, P. (2012). Rapid enhancement of touch from non-informative vision of the hand. *Neuropsychologia*, 50 (8), 1954–1960. https://doi.org/10.1016/j.neuropsychologia.2012.04.020

Cohen, J. (1988). *Statistical power analysis for the behavioral sciences*. New York, NY: Routledge.

Coq, J. O., & Xerri, C. (2000). Age-related alteration of the forepaw representation in the rat primary somatosensory cortex. *Neuroscience*, 99(3), 403-411. https://doi.org/10.1016/S0306-4522(00)00211-6

Cornsweet, T. N. (1962). The Staircase-Method in Psychophysics. *The American Journal of Psychology*, 75 (3), 485. https://doi.org/10.2307/1419876

David-Jürgens, M., Churs, L., Berkefeld, T., Zepka, R. F., & Dinse, H. R. (2008). Differential effects of aging on fore–and hindpaw maps of rat somatosensory cortex. *PLoS One*, 3 (10), e3399. https://doi.org/10.1371%2Fjournal.pone.0003399

Dinse, J., Härtwich, N., Waehnert, M., Tardif, C., Schäfer, A., Geyer, S., . . . Bazin, P.-L. (2015). A cytoarchitecture-driven myelin model reveals area-specific signatures in human primary and secondary areas using ultra-high resolution in-vivo brain MRI. *NeuroImage*, 114, 71–87. https://doi.org/10.1016/j.neuroimage.2015.04.023

Elbert, T., Pantev, C., Wienbruch, C., Rockstroh, B., & Taub, E. (1995). Increased cortical representation of the fingers of the left hand in string players. *Science*, 270 (5234), 305–307. https://doi.org/10.1126/science.270.5234.305

Feldman, D. E., & Brecht, M. (2005). Map plasticity in somatosensory cortex. *Science*, *310* (5749), 810-815. https://doi.org/10.1126/science.1115807

Ferezou, I., Haiss, F., Gentet, L. J., Aronoff, R., Weber, B., & Petersen, C. C. (2007). Spatiotemporal Dynamics of Cortical Sensorimotor Integration in Behaving Mice. *Neuron*, 56 (5), 907–923. https://doi.org/10.1016/j.neuron.2007.10.007

Florence, S. L., Jain, N., & Kaas, J. H. (1997). Plasticity of somatosensory cortex in primates. In *Seminars in Neuroscience*, 9 (1-2), 3-12. Academic Press. https://doi.org/10.1006/smns.1997.0101

Gescheider, G. A., Edwards, R. R., Lackner, E. A., Bolanowski, S. J., & Verrillo, R. T. (1996). The effects of aging on information-processing channels in the sense of touch: Iii. differential sensitivity to changes in stimulus intensity. *Somatosensory & Motor Research*, 13 (1), 73–80. https://doi.org/10.3109/08990229609028914

Geyer, S., Schleicher, A., & Zilles, K. (1999). Areas 3a, 3b, and 1 of Human Primary Somatosensory Cortex: 1. Microstructural Organization and Interindividual Variability. *NeuroImage*, 10 (1), 63–83. https://doi.org/10.1006/NIMG.1999.0440

Glasser, M. F., Coalson, T. S., Robinson, E. C., Hacker, C. D., Harwell, J., Yacoub, E., ... & Van Essen, D. C. (2016). A multi-modal parcellation of human cerebral cortex. *Nature*, *536* (7615), 171-178. https://doi.org/ 10.1038/nature18933

Glover, G. H., Li, T. Q., & Ress, D. (2000). Image‐based method for retrospective correction of physiological motion effects in fMRI: RETROICOR. *Magnetic Resonance in Medicine*, *44* (1), 162-167. https://doi.org/10.1002/1522-2594(200007)44:1%3C162::aid-mrm23%3E3.0.co;2-e

Godde, B., Berkefeld, T., David-Jürgens, M., & Dinse, H. R. (2002). Age-related changes in primary somatosensory cortex of rats: evidence for parallel degenerative and plastic-adaptive processes. *Neuroscience & Biobehavioral Reviews*, 26 (7), 743-752. https://doi.org/10.1016/S0149-7634(02)00061-1

Gryga, M., Taubert, M., Dukart, J., Vollmann, H., Conde, V., Sehm, B., . . . Ragert, P. (2012). Bidirectional gray matter changes after complex motor skill learning. *Frontiers in Systems Neuroscience*, 6, 37. https://doi.org/10.3389/fnsys.2012.00037

Haacke, E. M., Xu, Y., Cheng, Y. C. N., & Reichenbach, J. R. (2004). Susceptibility weighted imaging (SWI). *Magnetic Resonance in Medicine*, *52*(3), 612-618. https://doi.org/10.1002/mrm.20198

Haggard, P., Kitadono, K., Press, C., & Taylor-Clarke, M. (2006). The brain's fingers and hands. *Experimental Brain Research*, 172 (1), 94-102. https://doi.org/10.1007/s00221-005-0311-8

Hametner, S., Endmayr, V., Deistung, A., Palmrich, P., Prihoda, M., Haimburger, E., et al. (2018). The influence of brain iron and myelin on magnetic susceptibility and effective transverse relaxation - a biochemical and histological validation study. *NeuroImage* 179, 117–133. https://doi.org/10.1016/j.neuroimage.2018.06.007

Han, X., Pham, D. L., Tosun, D., Rettmann, M. E., Xu, C., & Prince, J. L. (2004). CRUISE: Cortical reconstruction using implicit surface evolution. *NeuroImage*, 23 (3), 997–1012. https://doi.org/10.1016/j.neuroimage.2004.06.043

Haroutunian, V., Katsel, P., Roussos, P., Davis, K. L., Altshuler, L. L., & Bartzokis, G. (2014). Myelination, oligodendrocytes, and serious mental illness. *Glia*, 62 (11), 1856–1877. https://doi.org/10.1002/glia.22716

Huber, L., Finn, E. S., Handwerker, D. A., Bönstrup, M., Glen, D. R., Kashyap, S., ... & Bandettini, P. A. (2020). Sub-millimeter fMRI reveals multiple topographical digit representations that form action maps in human motor cortex. *NeuroImage*, *208*, 116463. https://doi.org/10.1016/j.neuroimage.2019.116463

Huber, L., Uludağ, K., & Möller, H. E. (2019). Non-BOLD contrast for laminar fMRI in humans: CBF, CBV, and CMRO2. *NeuroImage*, *197*, 742-760. https://doi.org/10.1016/j.neuroimage.2017.07.041

Huntenburg, J. M., Bazin, P. L., Goulas, A., Tardif, C. L., Villringer, A., & Margulies, D. S. (2017). A systematic relationship between functional connectivity and intracortical myelin in the human cerebral cortex. *Cerebral Cortex*, 27 (2), 981-997. https://doi.org/10.1093/cercor/bhx030

In M-H, Posnansky O, Speck O. (2016). PSF mapping-based correction of eddy-current-induced distortions in diffusion-weighted echo-planar imaging. *Magnetic Resonance in Medicine*, 75, 2055–2063. https://doi.org/10.1002/mrm.25746

Jain, N., Catania, K. C., & Kaas, J. H. (1998). A histologically visible representation of the fingers and palm in primate area 3b and its immutability following long-term deafferentations. *Cerebral Cortex*, *8* (3), 227-236. https://doi.org/10.1093/cercor/8.3.227

Kalisch, T., Ragert, P., Schwenkreis, P., Dinse, H. R., & Tegenthoff, M. (2009). Impaired tactile acuity in old age is accompanied by enlarged hand representations in somatosensory cortex. *Cerebral Cortex*, 19 (7), 1530–1538. https://doi.org/10.1093/cercor/bhn190

Kalisch T., Tegenthoff M., & Dinse H. R. (2008). Improvement of sensorimotor functions in old age by passive sensory stimulation. *Clinical Interventions in Aging*, 3, 673–690. https://doi.org/10.2147/cia.s3174

Kelley, D. J., Oakes, T. R., Greischar, L. L., Chung, M. K., Ollinger, J. M., Alexander, A. L., ... & Davidson, R. J. (2008). Automatic physiological waveform processing for FMRI noise correction and analysis. *PloS one*, 3 (3), e1751. https://doi.org/10.1371/journal.pone.0001751

Kleiner, M., Brainard, D., Pelli, D., Ingling, A., Murray, R., & Broussard, C. (2007). What's new in psychtoolbox-3. *Perception*, 36 (14), 1–16. Retrieved from https://nyuscholars.nyu.edu/en/publications/whats-new-in-psychtoolbox-3

Kuehn, E., Dinse, J., Jakobsen, E., Long, X., Schäfer, A., Bazin, P. L., ... & Margulies, D. S. (2017a). Body topography parcellates human sensory and motor cortex. *Cerebral Cortex*, 27 (7), 3790-3805. https://doi.org/10.1093/cercor/bhx026

Kuehn E., Doehler J., Pleger B. (2017b). The influence of vision on tactile Hebbian learning. *Scientific Reports,* 7, 9069. https://doi.org/10.1038/s41598-017-09181-6

Kuehn, E., Haggard, P., Villringer, A., Pleger, B., & Sereno, M. I. (2018a). Visually-driven maps in area 3b. *Journal of Neuroscience*, 38 (5), 1295-1310. https://doi.org/10.1523/JNEUROSCI.0491-17.2017

Kuehn, E., Mueller, K., Turner, R., & Schütz-Bosbach, S. (2014). The functional architecture of S1 during touch observation described with 7 T fMRI. *Brain Structure and Function*, 219 (1), 119–140. https://doi.org/10.1007/s00429-012-0489-z

Kuehn, E., & Pleger, B. (2020). Encoding schemes in somatosensation: from micro-to meta-topography. *NeuroImage*, *223*, 117255. https://doi.org/10.1016/j.neuroimage.2020.117255

Kuehn, E., Perez-Lopez, M. B., Diersch, N., Döhler, J., Wolbers, T., & Riemer, M. (2018b). Embodiment in the aging mind. *Neuroscience & Biobehavioral Reviews*, *86*, 207-225. https://doi.org/10.1016/j.neubiorev.2017.11.016

Kuehn, E., & Sereno, M.I. (2018). Modelling the Human Cortex in Three Dimensions. *Trends in Cognitive Sciences, 22*, 1073-1075. https://doi.org/10.1016/j.tics.2018.08.010

Langkammer, C., Schweser, F., Krebs, N., Deistung, A., Goessler, W., Scheurer, E., et al. (2012). Quantitative susceptibility mapping (QSM) as a means to measure brain iron? A post mortem validation study. *NeuroImage,* 62, 1593–9. https://doi.org/10.1016/j.neuroimage.2012.05.049

Laskov, V. N. (1995). Coding of tactile stimulus amplitude by neuronal ensembles in the somatosensory cortex of the rat brain. *Neurophysiology*, 27 (2), 63–70. https://doi.org/10.1007/BF01305374

Lazar, L., Chand, P., Rajan, R., Mohammed, H., & Jain, N. (2020). Somatosensory cortex of macaque monkeys is designed for opposable thumb. *Cerebral Cortex*, bhac061. https://doi.org/10.1093/cercor/bhac061

Liu, P., Chrysidou, A., Doehler, J., Hebart, M. N., Wolbers, T., & Kuehn, E. (2021). The organizational principles of de-differentiated topographic maps in somatosensory cortex. *Elife*, *10*, e60090. https://doi.org/10.7554/eLife.60090

Lohmann, G., Loktyushin, A., Stelzer, J., & Scheffler, K. (2018). Eigenvector centrality mapping for ultrahigh resolution fMRI data of the human brain. *biorxiv*, 494732. https://doi.org/https://doi.org/10.1101/494732

Lohmann, G., Müller, K., Bosch, V., Mentzel, H., Hessler, S., Chen, L., Zysset, S., & von Cramon, D. Y. (2001). LIPSIA--a new software system for the evaluation of functional magnetic resonance images of the human brain. *Computerized Medical Imaging and Graphics*, *25* (6), 449–457. https://doi.org/10.1016/s0895-6111(01)00008-8

Lucas, B. C., Bogovic, J. A., Carass, A., Bazin, P.-L., Prince, J. L., Pham, D. L., & Landman, B. A. (2010). The Java Image Science Toolkit (JIST) for rapid prototyping and publishing of neuroimaging software. *Neuroinformatics*, 8 (1), 5–17. https://doi.org/10.1007/s12021-009-9061-2

Mair, P. & Wilcox, R. (2018). Robust Statistical Methods Using WRS2. 0.10-0. Retrieved from https://cran.r-project.org/web/packages/WRS2/vignettes/WRS2.pdf

Mao, T., Kusefoglu, D., Hooks, B. M., Huber, D., Petreanu, L., & Svoboda, K. (2011). Long-Range Neuronal Circuits Underlying the Interaction between Sensory and Motor Cortex. *Neuron*, 72 (1), 111–123. https://doi.org/10.1016/j.neuron.2011.07.029

Marques, J. P., Kober, T., Krueger, G., van der Zwaag, W., Van de Moortele, P.-F., & Gruetter, R. (2010). MP2RAGE, a self bias-field corrected sequence for improved segmentation and T1-mapping at high field. *NeuroImage*, 49 (2), 1271–1281. https://doi.org/10.1016/j.neuroimage.2009.10.002

McAuliffe, M., Lalonde, F., McGarry, D., Gandler, W., Csaky, K., & Trus, B. (2001). Medical Image Processing, Analysis and Visualization in clinical research. In Proceedings 14th ieee symposium on computer-based medical systems (pp. 381–386). *IEEE Computer Soc*iety https://doi.org/10.1109/CBMS.2001.941749

Meyer, H. S., Egger, R., Guest, J. M., Foerster, R., Reissl, S., & Oberlaender, M. (2013). Cellular organization of cortical barrel columns is whisker-specific. *Proceedings of the National Academy of Sciences*, *110* (47), 19113-19118. https://doi.org/10.1073/pnas.13126911

Mücke, M., Cuhls, H., Radbruch, L., Baron, R., Maier, C., Tölle, T., . . . Rolke, R. (2014). Quantitative sensorische Testung. *Schmerz*, 28, 635–648. https://doi.org/10.1007/s00482-014-1485-4

Muret, D., Root, V., Kieliba, P., Clode, D., & Makin, T. R. (2022). Beyond body maps: Information content of specific body parts is distributed across the somatosensory homunculus. *Cell Reports*, *38* (11), 110523. https://doi.org/10.1016/j.celrep.2022.110523

Northall, A., Doehler, J., Weber, M., Vielhaber, S., Schreiber, S., & Kuehn, E. (2022). Topographic Stability and Layer-Specific Flexibility are Mechanisms of Human Cortical Plasticity. *bioRxiv*, 2022.05.29.493865. https://doi.org/10.1101/2022.05.29.493865

Oldfield, R. C. (1971). The assessment and analysis of handedness: The Edinburgh inventory. *Neuropsychologia*, 9 (1), 97–113. https://doi.org/10.1016/0028-3932(71)90067-4

Pelli, D. G. (1997). The VideoToolbox software for visual psychophysics: transforming numbers into movies. *Spatial Vision*, 10 (4), 437–42.

Peters, A. (2009). The effects of normal aging on myelinated nerve fibers in monkey central nervous system. *Frontiers in Neuroanatomy*, 11. https://doi.org/10.3389/neuro.05.011.2009

Petersen, C. C. (2007). The functional organization of the barrel cortex. *Neuron*, 56 (2), 339–355. https://doi.org/10.1016/j.neuron.2007.09.017

Petersen, C. C. & Crochet, S. (2013). Synaptic Computation and Sensory Processing in Neocortical Layer 2/3. *Neuron*, 78 (1), 28–48. https://doi.org/10.1016/j.neuron.2013.03.020

Pleger, B., Dinse, H. R., Ragert, P., Schwenkreis, P., Malin, J. P., & Tegenthoff, M. (2001). Shifts in cortical representations predict human discrimination improvement. *Proceedings of the National Academy of Sciences of the United States of America*, 98 (21), 12255–60. https://doi.org/10.1073/pnas.191176298

Pleger, B., Wilimzig, C., Nicolas, V., Kalisch, T., Ragert, P., Tegenthoff, M., & Dinse, H. R. (2016). A complementary role of intracortical inhibition in age-related tactile degradation and its remodelling in humans. *Scientific Reports*, 6 (27388), 1–15. https://doi.org/10.1038/srep27388

Pielecka-Fortuna, J., Wagener, R. J., Martens, A. K., Goetze, B., Schmidt, K. F., Staiger, J. F., & Löwel, S. (2015). The disorganized visual cortex in reelin-deficient mice is functional

and allows for enhanced plasticity. *Brain Structure and Function*, 220 (6), 3449-3467. https://doi.org/10.1007/s00429-014-0866-x

Puckett A. M., Bollmann S., Junday K., Barth M., & Cunnington R. (2020). Bayesian population receptive field modeling in human somatosensory cortex. *NeuroImage,* 208, 116465. https://doi.org/10.1016/j.neuroimage.2019.116465

Qi, H., & Kaas, J.H. (2004). Myelin stains reveal an anatomical framework for the representation of the digits in somatosensory area 3b of macaque monkeys. *Journal of Comparative Neurology, 477*. https://doi.org/10.1002/cne.20247

Ragert, P., Schmidt, A., Altenmüller, E., & Dinse, H. R. (2004). Superior tactile performance and learning in professional pianists: Evidence for meta-plasticity in musicians. *European Journal of Neuroscience*, 19 (2), 473–478. https://doi.org/10.1111/j.0953816X.2003.03142.x

Schweisfurth M. A., Frahm J, & Schweizer R. (2015). Individual left-hand and right-hand intra-digit representations in human primary somatosensory cortex. *European Journal of Neuroscience*. https://doi.org/10.1111/ejn.12978

Schweisfurth M. A., Schweizer R., & Frahm J. (2011). Functional MRI indicates consistent intra-digit topographic maps in the little but not the index finger within the human primary somatosensory cortex. *NeuroImage*, 56, 2138–2143. https://doi.org/10.1016/j.neuroimage.2011.03.038

Schweisfurth M. A., Schweizer R., & Treue S. (2014). Feature-based attentional modulation of orientation perception in somatosensation. *Frontiers in Human Neuroscience,* 8, 519. https://doi.org/10.3389/fnhum.2014.00519

Schwenkreis, P., El Tom, S., Ragert, P., Pleger, B., Tegenthoff, M., & Dinse, H. R. (2007). Assessment of sensorimotor cortical representation asymmetries and motor skills in violin players. *European Journal of Neuroscience*, 26 (11), 3291–3302. https://doi.org/10.1111/j.1460-9568.2007.05894.x

Sereno, M. I. (2005). Plasticity and its limits. *Nature*, 435 (7040), 288–289. https://doi.org/10.1038/435288a

Sereno, M. I., Sood, M. R., & Huang, R. S. (2022). Topological maps and brain computations from low to high. *Frontiers in Systems Neuroscience*, 43. https://doi.org/10.3389/fnsys.2022.787737

Sethian, J. A. (1999). Level set methods and fast marching methods: evolving interfaces in computational geometry, fluid mechanics, computer vision, and materials science (Vol. 3). Cambridge University Press.

Sherman, S. M. (2016). Thalamus plays a central role in ongoing cortical functioning. *Nature Neuroscience*, 19 (4), 533. https://doi.org/10.1038/nn.4269

Snaidero, N., Schifferer, M., Mezydlo, A., Zalc, B., Kerschensteiner, M., & Misgeld, T. (2020). Myelin replacement triggered by single-cell demyelination in mouse cortex. *Nature Communications*, *11* (1), 1-12. https://doi.org/10.1038/s41467-020-18632-0

Shoham, D., & Grinvald, A. (2001). The cortical representation of the hand in macaque and human area SI: high resolution optical imaging. *Journal of Neuroscience*, *21* (17), 6820-6835. https://doi.org/10.1523%2FJNEUROSCI.21-17-06820.2001

Spengler, F., Godde, B., & Dinse, H. R. (1995). Effects of ageing on topographic organization of somatosensory cortex. *Neuroreport,* 6 (3), 469-73. https://doi.org/10.1097/00001756-199502000-00016

Stüber, C., Morawski, M., Schäfer, A., Labadie, C., Wähnert, M., Leuze, C., . . . Turner, R. (2014). Myelin and iron concentration in the human brain: A quantitative study of mri contrast. *NeuroImage*, 93, 95–106. https://doi.org/10.1016/j.neuroimage.2014.02.026

Sullivan, B. & Kaszynski, A (2019). PyVista: 3D plotting and mesh analysis through a streamlined interface for the Visualization Toolkit (VTK). *Journal of Open Source Software*, 4 (37), 1450, https://doi.org/10.21105/joss.01450

Sullivan, L. M., Weinberg, J., & Keaney Jr, J. F. (2016). Common statistical pitfalls in basic science research. *Journal of the American Heart Association*, *5* (10), e004142. https://doi.org/10.1161/jaha.116.004142

Tardif, C. L., Schäfer, A., Waehnert, M., Dinse, J., Turner, R., & Bazin, P.-L. (2015). Multi-contrast multi-scale surface registration for improved alignment of cortical areas. *NeuroImage*, 111, 107–122. https://doi.org/10.1016/j.neuroimage.2015.02.005

Thornbury, J. M. & Mistretta, C. M. (1981). Tactile sensitivity as a function of age. *Journal of Gerontology*, 36 (1), 34–39. https://doi.org/10.1093/geronj/36.1.34

Tosun, D., Rettmann, M. E., Han, X., Tao, X., Xu, C., Resnick, S. M., . . . Prince, J. L. (2004). Cortical surface segmentation and mapping. *NeuroImage*, 23, 108–18. https://doi.org/10.1016/j.neuroimage.2004.07.042

Viaene, A. N., Petrof, I., & Sherman, S. M. (2011). Synaptic properties of thalamic input to layers 2/3 and 4 of primary somatosensory and auditory cortices. *Journal of Neurophysiology*, 105 (1), 279–292. https://doi.org/10.1152/jn.00747.2010

Vieluf, S., Godde, B., Reuter, E.-M., & Voelcker-Rehage, C. (2013). Age-related differences in finger force control are characterized by reduced force production. *Experimental Brain Research*, 224 (1), 107–117. https://doi.org/10.1007/s00221-012-3292-4

Voelcker-Rehage, C. & Alberts, J. L. (2005). Age-related changes in grasping force modulation. *Experimental Brain Research*, 166 (1), 61–70. https://doi.org/10.1007/s00221-005-2342-6

Vogt, C., & Vogt, O. (1919). *Allgemeine ergebnisse unserer hirnforschung* (Vol. 21). JA Barth.

Waehnert, M., Dinse, J., Weiss, M., Streicher, M., Waehnert, P., Geyer, S., . . . Bazin, P.-L. (2014). Anatomically motivated modeling of cortical laminae. *NeuroImage*, 93, 210–220. https://doi.org/10.1016/j.neuroimage.2013.03.078

Welker C. (1976). Receptive fields of barrels in the somatosensory neocortex of the rat. *Journal of Computational Neurology*, 166, 173–189. https://doi.org/10.1002/cne.901660205

Welker C., Woolsey, T. A. (1974). Structure of layer IV in the somatosensory neocortex of the rat: description and comparison with the mouse. *Journal of Computational Neurology*, 158 (4), 437–453. https://doi.org/10.1002/cne.901580405

Wesselink, D. B., Sanders, Z. B., Edmondson, L. R., Dempsey-Jones, H., Kieliba, P., Kikkert, S., Themistocleous, A. C., Emir, U., Diedrichsen, J., Saal, H. P., & Makin, T. R. (2022). Malleability of the cortical hand map following a finger nerve block. *Science Advances*, *8* (16), eabk2393. https://doi.org/10.1126/sciadv.abk2393

Woolsey, T.A., & van der Loos, H. (1970). The structural organization of layer IV in the somatosensory region (SI) of mouse cerebral cortex. The description of a cortical field composed of discrete cytoarchitectonic units. *Brain Research,* 17 (2), 205-42. https://doi.org/10.1016/0006-8993(70)90079-x

Wu, J., Dong, R., Smutz, W., & Rakheja, S. (2003). Dynamic interaction between a fingerpad and a flat surface: experiments and analysis. *Medical Engineering & Physics*, 25 (5), 397–406. https://doi.org/10.1016/S1350-4533(03)00035-3

Yousry, T. A., Schmid, U. D., Alkadhi, H., Schmidt, D., Peraud, A., Buettner, A., & Winkler, P. (1997). Localization of the motor hand area to a knob on the precentral gyrus. A new landmark. *Brain*, *120* (1), 141-157. https://doi.org/10.1093/brain/120.1.141

Yu, Y., Huber, L., Yang, J., Jangraw, D. C., Handwerker, D. A., Molfese, P. J., ... & Bandettini, P. A. (2019). Layer-specific activation of sensory input and predictive feedback in the human primary somatosensory cortex. *Science Advances*, *5* (5), eaav9053. https://doi.org/10.1126/sciadv.aav9053

Zeidman P., Silson E. H., Schwarzkopf D. S., Baker C. I., & Penny W. (2018). Bayesian population receptive field modelling. *NeuroImage* 180, 173–187. https://doi.org/10.1016/j.neuroimage.2017.09.008

Zhang, Z. W. & Deschênes, M. (1997). Intracortical axonal projections of lamina VI cells of the primary somatosensory cortex in the rat: a single-cell labeling study. *The Journal of Neuroscience*, 17 (16), 6365–79. https://doi.org/10.1523/jneurosci.17-16-06365.1997

Zheng, W., Nichol, H., Liu, S., Cheng, Y.-C.N., Haacke, E.M., 2013. Measuring iron in the brain using quantitative susceptibility mapping and X-ray fluorescence imaging. *NeuroImage* 78, 68–74. https://doi.org/10.1016/j.neuroimage.2013.04.022

Zhi, D., King, M., Hernandez-Castillo, C. R., & Diedrichsen, J. (2022). Evaluating brain parcellations using the distance-controlled boundary coefficient. *Human Brain Mapping*, 10.1002/hbm.25878. https://doi.org/10.1002/hbm.25878